Evaluating the potential of aerial remote sensing in flue-cured tobacco

Austin Craig Hayes

Thesis submitted to the faculty of Virginia Polytechnic Institute and State University

in partial fulfillment of the requirements for the degree of

Master of Science

in

Crop and Soil Environmental Sciences

T. David Reed

Charles S. Johnson

David S. McCall

April 19, 2019

Blackstone, VA

Keywords: remote sensing, flue-cured tobacco, unmanned aerial vehicle, UAV, ENDVI, vegetation index, nitrogen, black shank, *Phytophthora nicotianae*, hyperspectral imagery

Evaluating the potential of aerial remote sensing in flue-cured tobacco

Austin Craig Hayes

ABSTRACT

Flue-cured tobacco (*Nicotiana tabacum* L.) is a high value-per-acre crop that is intensively managed to optimize the yield of high quality cured leaf. Aerial remote sensing, specifically unmanned aerial vehicles (UAVs), present flue-cured tobacco producers and researchers with a potential tool for scouting and crop management. A two-year study, conducted in Southside Virginia at the Southern Piedmont Agricultural Research and Extension Center and on commercial farms, assessed the potential of aerial remote sensing in flue-cured tobacco. The effort encompassed two key objectives. First, examine the use of the enhanced normalized difference vegetation index (ENDVI) for separating flue-cured tobacco varieties and nitrogen rates. Secondly, develop hyperspectral indices and/or machine learning classification models capable of detecting *Phytophthora nicotianae* (black shank) incidence in flue-cured tobacco. In 2017, UAV-acquired ENDVI surveys demonstrated the ability to consistently separate between flue-cured tobacco varieties and nitrogen rates from topping to harvest. In 2018, ENDVI revealed significant differences among N-rates as early as 34 days after transplanting. Two hyperspectral indices were developed to detect black shank incidence based on differences in the spectral profiles of asymptomatic flue-cured tobacco plants compared to those with black shank symptoms. Testing of the indices showed significant differences between the index values of healthy and symptomatic plants (*alpha* = 0.05). In addition, the indices were able to detect black shank symptoms pre-symptomatically (*alpha* = 0.09). Subspace linear discriminant analysis, a machine learning classification, was also used for prediction of black shank incidence with up to 85.7% classification accuracy.

Evaluating the potential of aerial remote sensing in flue-cured tobacco

Austin Craig Hayes

General Audience Abstract

Unmanned Aerial Vehicle's (UAVs) or drones, as they are commonly referred to, may have potential as a tool in flue-cured tobacco research and production. UAVs combined with sensors and cameras provide the opportunity to gather a large amount of data on a particular crop, which may be useful in crop management. Given the intensive management of flue-cured tobacco, producers may benefit from extra insight on how to better assess threats to yield such as under-fertilization and disease pressure. A two-year study was conducted in Southside Virginia at the Southern Piedmont Agricultural Research and Extension Center and on commercial farms. There were two objectives to this effort. First, assess the ability of UAV-acquired multispectral near-infrared imagery to separate flue-cured tobacco varieties and nitrogen rates. Secondly, develop hyperspectral indices and machine learning models that can accurately predict the incidence of black shank in flue-cured tobacco. Flue-cured tobacco nitrogen rates were significantly different in 2017 from 59 days after transplanting to harvest using UAV-acquired near-infrared imagery. In 2018, heavy rainfall may have led to nitrogen leaching from the soil resulting in nitrogen rates being significantly different as early as 34 days after transplanting. The imagery also showed a significant relationship with variety maturation type in the late stages of crop development during ripening. Two hyperspectral indices were developed and one machine learning model was trained. Each had the ability to detect black shank incidence in flue-cured tobacco pre-symptomatically, as well as separated black shank infested plants from healthy plants.

Acknowledgements

I am exceedingly grateful to the many people who supported me and made it possible for me to pursue an M.S. degree at Virginia Tech. I would like to thank Dr. David Reed, for having the confidence in me to allow me take on research that challenged me and met my interests. He has been exceptionally supportive and helpful throughout this entire process, and I could not have completed this degree without him. I would also like to thank Dr. Charles Johnson for the advice and wisdom he provided me. I would like to thank Dr. David McCall, for his participation in this project and the time and knowledge he shared with me over these two years.

I would like to thank Grant Coffee, Ned Jones, the agronomy team, and the field crew at Southern Piedmont AREC for their work maintaining the plots that I studied and for making me laugh. I would also like to thank Melody McGhee and Margaret Kenny for providing support and assistance during my time here. I would like to thank Pat Donovan, for the immense amount of assistance she provided me in learning GIS software and her willingness to drop everything to help me. I would like to thank my professors and fellow students in Blacksburg, as well as all the other faculty, staff, and graduate students at Southern Piedmont AREC, for the support they offered. I would like to thank Altria Client Services for the funding necessary to make this project possible. I am truly grateful to Amrita Sahu and the rest of the hyperspectral imaging group at Altria for providing me with a vast amount of knowledge and support with machine learning and hyperspectral data.

I would like to thank my parents, Brian and Wanda Hayes, for their wisdom, prayers, and encouragement. I would also like to thank my siblings, grandparents, and extended family for backing me throughout graduate school. Finally, I would like to thank my wife, Brigette Hayes, for her unwavering love, support, and encouragement through this entire process.

Contents

List of Figures

List of Tables

List of Appendices

Chapter I

Introduction

Unmanned aerial vehicles, commonly referred to as drones, have been used in military operations for several decades. However, in recent years, the increased availability and reduced costs of small UAVs has made them a disruptive technology for many industries such as construction, aerial inspection, mapmaking, forestry, and environmental science. Agriculture has also benefited from UAV technology, primarily as a scouting method. According to the Massachusetts Institute of Technology, agricultural drones are one of the top ten breakthrough technologies (Anderson, 2014). UAVs enable growers and researchers the ability to rapidly scout large tracts of land. If a near-infrared camera is equipped on the drone, maps can be made that indicate plant health throughout a field. This enhances the scouting ability of UAV operators further by allowing them to more easily locate problem areas and display that information later to interested parties. While UAVs can assist in agricultural scouting, growers are most interested in obtaining actionable insights from UAV imagery. There is potential for UAVs to be used as part of a precision management system. However, variations among different crops and varieties can make applications specific and not transferrable to other cropping applications.

Precision agriculture and smart farming have become increasingly popular practices. Traditionally, fields were cultivated and managed as one management unit. The same inputs, in the form of seed, fertilizer, pesticides, and irrigation, were distributed evenly throughout the field. While these traditional methods of evenly distributed inputs still persist today, many crop producers have opted to implement management zones in order to more precisely apply crop inputs. A field's management zones are often delineated by soil type surveys, grid soil sampling, and previous year's yield data. Growers can increase input efficiency by applying more in areas

where the inputs are most needed and less in areas where they are less needed, leading to improved farm profitability (Zhang, Wang, & Wang, 2002). Variable rate sprayers and fertilizer spreaders, powered by GPS, are used to distribute the unique input requirements of each management zone.

Management zones are a strategy to mitigate large-scale variations in cropping systems, however, small variations may still exist within the management zones themselves. To eliminate this variability, field data with more spatial resolution is needed. Spatial resolution in precision agriculture can be defined as the number of data points in a given area. To illustrate, if a field that had 4 management zones was split into 8 management zones it would double the spatial resolution of the management map. Increasing the spatial resolution of a precision management plan can increase resource use efficiency. However, time and resources are necessary to gather the extra data. If we were to manage a field on an individual plant level, this efficiency would be maximized. Yet, it is impractical to do this using traditional methods, such as soil sampling.

UAVs provide the ability to gather data on crops at a spatial resolution exceeding the individual plant level. The data are collected at an extremely fast rate, when compared to traditional methods and this collection of data is repeatable. Furthermore, traditional data used in creating management zone maps (soil tests, yield data) is either derived from soil properties or previous crops. UAVs collect data from the current crop being cultivated. Although UAV use in precision management systems is still in the early stages, it has potential to be used as a tool in crop management (Mogili & Deepak, 2018).

References

Anderson, C. (2014). Agricultural Drones. *MIT Technology Review*, *117*(3): 58-60.

Mogili, U. M., & Deepak, B. B. V. L. (2018). Review on application of drone systems in precision agriculture. *Procedia Computer Science*, *133*: 502-509.

Zhang, N., Wang, M., & Wang, N. (2002). Precision agriculture: a worldwide overview. *Computers and Electronics in Agriculture*, *36*: 113-132.

Chapter II

Literature Review

Remote Sensing in Agriculture

Remote sensing is a process for studying the earth's surface. According to the USGS ("What is Remote Sensing", n.d.), "remote sensing is the process of detecting and monitoring the physical characteristics of an area by measuring its reflected and emitted radiation at a distance from the targeted area." Remote sensing applications in plant science typically involve measuring the reflectance of electromagnetic radiation from soil or plant matter (Mulla, 2013). The electromagnetic spectrum (Fig. 2.1) consists of ranges of energy with various wavelength, frequency, and energy. Remote sensing research in agriculture and environmental science often uses information from the visible, infrared, and ultra-violet ranges of the electromagnetic spectrum (Mulla, 2013).

In the visible range, three subranges, or bands, exist: blue, green, and red. Plants absorb large amounts of radiation in the blue and red portion of the visible spectrum (Pinter *et al*., 2003). Chlorophyll absorbs this radiation for energy use in photosynthesis. In the green band, plants absorb comparatively less radiation. The radiation that is not absorbed by a surface is reflected. Therefore, reflectance is the opposite of absorbance, with plants reflecting more energy in the green band when compared with red and blue (Fig. 2.2). This is why we see plants as green.

Infrared radiation is the range of electromagnetic energy just beyond the red band of visible light, with longer wavelengths and lower energy. Near-infrared (NIR) radiation is the band closest to the visible range, with the shortest wavelengths in the infrared range. Shortwave-

Infrared (SWIR), Midwave-Infrared (MWIR), and Longwave Infrared (LWIR) radiation are the other bands in the infrared range, with increasing wavelengths. Plants reflect a high amount of NIR radiation (Fig. 2.2.) because the energy contained in this range is too low to be used in photosynthesis (Smith *et al*., 2010). This contrast in reflectance of NIR to red and blue portions of the electromagnetic spectrum is the basis for nearly every vegetation index used in remote sensing for plant science (Sripada, Heiniger, White, & Weisz, 2006). To illustrate this, below are some of the most common vegetation indices.

$$Difference\ Vegetation\ Index = NIR - Red$$ (Tucker, 1979)

$$Simple\ Ratio\ Index = \frac{NIR}{Red}$$ (Birth & McVey, 1968)

$$Normalized\ Difference\ Vegetation\ Index = \frac{NIR-Red}{NIR+Red}$$ (Rouse, 1973)

$$Enhanced\ Normalized\ Difference\ Vegetation\ Index = \frac{(NIR+Green)-(2\times Blue)}{(NIR+Green)+(2\times Blue)}$$

("Maxmax", 2015)

There are several platforms for measuring electromagnetic radiation, including satellites, aircraft, and vehicle-mounted or handheld sensors. The first Landsat satellite was launched in 1972, providing researchers open access to geospatial imagery. In the decades following this launch, researchers in environmental science and forestry used Landsat imagery to study the earth's surface over large landmasses (Zhang *et al*., 2003; Jewel, 1989). Bhatti, Mulla, and Frazier (1991) conducted one of the first studies to investigate the use of Landsat imagery to predict measureable factors in cropping systems. Their study showed that Landsat imagery had potential as a means to spatially estimate soil organic matter, soil phosphorus, and crop yield potential.

Satellite imagery data provides researchers an excellent medium to study vegetation and the environment at a regional and global scale. However, using satellite data for precision agriculture applications has several disadvantages. First, satellite imagery has a lower spatial resolution when compared to aircraft acquired imagery (Moran, Inoue, & Barnes, 1997). Spatial resolution, which is an important concept in remote sensing, is defined as the area represented by each pixel in an image. The current spatial resolution of Landsat is 30 meters (Mulla, 2013). This means that each pixel of a Landsat image represents a 30 x 30 meter square. This spatial resolution is too coarse to provide data with adequate precision necessary to be used in most agricultural settings; certainly not in tobacco. Recently launched proprietary satellites such as GeoEye and WorldView, provide sub-meter spatial resolutions (Mulla, 2013). However, the data from these satellites can be cost prohibitive and is still more course than aircraft acquired imagery. The second problem with satellite imagery is the lack of repeatability. Satellites only acquire imagery from a given area of the globe several times per month. Furthermore, if cloud cover is present it would render the imagery unusable for crop analysis (Moran *et al*., 1997).

Manned aircraft, such as helicopters and small airplanes, are another platform for acquisition of aerial imagery for use in crop research. In fact, the use of manned aircraft to gather aerial imagery of crops for research purposes pre-dates the use of satellites (Brockie, 1956). Many of these early studies involved a qualitative analysis of cropping systems from the air using visible range photographs. Digital imagery from satellite data in the 1970's prompted the invention of a wide variety of vegetation indices, such as the normalized difference vegetation index (NDVI), for quantifying image features based on plant health and photosynthetic activity. This shift from analyzing images qualitatively to using indices to mathematically analyze imagery spawned a new era of remote sensing research. These indices were tested by crop

science researchers using manned aircraft acquired imagery. Shanahan *et al*. (2001) used aerial imagery to predict corn grain yield. Clay, Kim, Chang, Clay, and Dalsted (2006) explored the ability of vegetation indices to characterize water and nitrogen stress in corn. A wide variety of uses for digital imagery and vegetation indices have been explored using imagery taken by manned aircraft, including: mapping of weed pressure (Lamb & Brown, 2001), insect pest stress (Dupont, Campenella, Seal, Willers, & Hood, 2000), and a number of other soil and plant properties (Christy, 2008; Corwin & Lesch, 2003).

Researchers are able to analyze cropping systems with higher spatial resolution by using aircraft (Moran, 1997). Spatial resolution is the major advantage of aircraft derived imagery, sometimes referred to as low-altitude remote sensing. Another advantage of using aircraft is the control over when the imagery is taken. Satellites limit the user to the date and time that the satellite was in orbit over the area of interest (Moran, 1997). This may not line up with the goals of the research, and repeated images may not be possible at the same time of day. Furthermore, as previously discussed, cloud cover can ruin the usability of satellite acquired imagery. By using low-altitude remote sensing in the form of a manned aircraft, timing is controlled and cloud cover is not an issue. The main disadvantage of manned aircraft is cost. While Landsat imagery is free, access to a helicopter or plane has a high cost, along with the fuel cost for operating the aircraft. The total cost of obtaining aerial imagery using manned aircraft certainly precludes the possibility of it being widely used by farmers for scouting and crop analysis.

Unmanned Aerial Vehicles (UAVs) offer today's researchers and growers a valuable tool with which to collect remote sensing data (Honrado *et al*., 2017). Though used in military operations for decades (Cargill, 2014), UAVs have only recently become a cost effective product for civilian use. They offer high spatial resolution, relatively low cost, and an increasing number

of user friendly software applications that manage flight control and imagery post-processing (Honrado *et al*., 2017). This has resulted in a number of crop science studies using UAVs over the past decade. Duan, Chapman, Guo, and Zheng (2017) showed that UAV acquired NIR imagery and the Normalized Difference Vegetation Index (NDVI) could predict wheat yield, indicating potential for high-throughput phenotyping by plant breeders. Similarly, Gong *et al*. (2018) predicted rapeseed yield. Liu *et al*. (2018), Li *et al*. (2018), and Caturegli *et al*. (2016) used UAVs and vegetation indices to diagnose nitrogen status of winter oilseed rape, rice, and turfgrass, respectively. UAVs, when combined with NIR vegetation indices, also have shown the ability to detect and quantify severity of a number of crop diseases. In potatoes, UAVs have been used to collect imagery to evaluate late blight severity (Duarte-Carvajalino *et al*., 2018). In Zhang *et al*. (2018), UAVs were used to detect sheath blight in rice. Di Gennaro *et al*. (2016) showed that NDVI surveys taken with UAVs were highly correlated with the presence of grape leaf stripe disease. Sankaran, Quirós, Knowles, and Knowles (2017) and Zhao *et al*. (2018) used UAVs to accurately detect emergence in potatoes and rapeseed, respectively. An important note is that, in all of these studies, a vegetation index or model is used by the researcher that allows for correlation to plant factors. The significance of the UAV is in providing the researchers with the spatial resolution to use the indices or models with the precision necessary to analyze imagery at the scale needed for cropping systems (Honrado *et al*., 2017).

Remote Sensing in Tobacco

Significantly fewer studies have been conducted investigating the potential benefits of UAVs and remote sensing in tobacco cultivation. Svotwa, Masuka, Maasdorp, and Murwira (2014) reported that broad-band (multispectral) NDVI observed no significant differences among different flue-cured tobacco varieties and nitrogen rates in the early-season. However, strong

differences appeared, for both, later in the season, as chlorophyll levels declined and the tobacco is ripened. The results from this study demonstrate that there is a potential benefit to using UAVs and NDVI to scout tobacco in the late growing stages. Additionally, multispectral NDVI has been shown to predict the nitrogen content of tobacco float-tray seedlings (Svotwa, Maasdorp, Murwira, & Masuka, 2012). Using deep neural networks, a machine learning classification, Fan, Lu, Gong, Xie, and Goodman (2018) were able to develop an algorithm to automatically detect tobacco plants in the field.

Although less is known about how UAVs and remote sensing may benefit tobacco growers and researchers, uses for the technology in so many other crops is promising. Tobacco is one of Virginia's top cash crops (VDACS, 2016). Furthermore, from a value per acre standpoint, tobacco is extremely valuable compared to other major crops like corn, soybeans, or small grains. That explains why growers would be interested in any tool that could gather more information on tobacco to help them more intensively and precisely manage their tobacco crop and protect leaf quality and yield.

Several major differences exist when comparing tobacco with grain and oilseed crops. These differences must be taken into consideration when thinking about how remote sensing can be used to analyze tobacco. One significant difference is the effects of nitrogen fertilization rates on yield and quality. In corn, nitrogen availability is positively related to yield (Biswas, Ma, & Navabi, 2016). In soils with more available nitrogen, corn is able to grow more vigorously with increased photosynthetic activity or energy production, storing more of that energy in the form of grain. NDVI, a plant health and vigor index, will then have higher values for those plants with higher nitrogen fertilization, all other things equal. Supporting this logic, researchers have been able to use NDVI to predict corn grain yield (Sharma, Honggang, Denton, & Franzen 2015).

There is interest in using early-season NDVI surveys to apply remedial variable rate fertilizer applications to decrease yield variability in crops.

If tobacco receives inadequate nitrogen, it will have low yield and poor quality. Over-fertilization, however, is more likely to occur (Reed, Johnson, Wilkinson, & Barts, 2019). Tobacco responds poorly to higher than average nitrogen rates. It is necessary for tobacco to deplete the soil of available nitrogen, during the growing season, in order for the leaves to naturally ripen, or "yellow". Therefore, excess nitrogen application will result in a crop that stays green, leading to a poor quality cured leaf that takes longer to cure (Reed *et al.*, 2019). Further, over-fertilization does not provide a significant yield increase. This makes it hard to measure tobacco leaf yield using the logic employed for predicting yield in grain and oilseed crops. In Svotwa *et al.* (2014), significance differences in NDVI values occurred when comparing flue-cured tobacco varieties and nitrogen rates once leaf ripening had begun. The nitrogen rate had a positive relationship with NDVI, suggesting that the soil receiving the least nitrogen was depleted the earliest, promoting leaf ripening. This earlier leaf ripening resulted in lower NDVI values, compared to the treatments that received a higher nitrogen rate. However, these differences only appeared at 10 weeks after transplanting. Due to tobacco's need to purge the topsoil of available nitrogen, 10 week's after planting is too late to apply a remedial variable rate nitrogen application.

Another difference between tobacco and crops like corn, soybean, and wheat is row spacing. Because of cultivation practices in tobacco, it has a significantly wider row spacing when compared to most other major row-crops. This must be taken into account when analyzing aerial tobacco surveys. The row spacing of crops is one factor that determines canopy closure (Hock, Knezevic, Martin, & Lindquist, 2009; Bradley, 2006). Grain and oilseed crops achieve

canopy closure relatively early in development. This allows for the entire area of the crop to be diagnosed with limited soil interference. Areas of the field that do contain pixels attributed to soil show incomplete canopy closure, which indicates a problem area that can be shown by NDVI. Conversely, tobacco does not achieve canopy closure between rows even in the late stages of plant development. This delayed canopy closure results in strips of bare soil in-between each row of plant matter when tobacco is viewed with aerial imagery. The soil features in-between each row can make it more difficult to assess NDVI surveys both qualitatively and quantitatively.

Hyperspectral Remote Sensing of Tobacco

Multispectral measurements, specifically NDVI, are more likely to be indicative of overall plant health and not specific plant stresses or leaf chemistry variations, because the wide bands of the spectrum that are measured with multispectral instruments do not pick up on subtle variations that exist between individual wavelengths. Furthermore, in higher plants, chlorophyll content is the principle force behind changes in NDVI, due to the effect of chlorophyll content on reflectance at and around 700 nm (Carter & Knapp, 2001). Hyperspectral data has much higher spectral resolution when compared to multispectral data. This allows indices to be tested that utilize very narrow bands of the electromagnetic spectrum (Mulla, 2013). Hyperspectral indices often use similar equations as multispectral indices such as Simple Ratio (SR) and NDVI. However, hyperspectral indices replace the mean band reflectance values (blue, green, red, and NIR) used by multispectral indices with mean narrow band values and often distinct wavelength reflectance values.

Researchers are able to relate spectral characteristics to more specific plant properties using hyperspectral reflectance measurements. In tobacco, several studies have been published with this objective in mind. Flue-cured tobacco leaf nitrogen content (LNC) has been related to

the wavelengths 570 nm and 670 nm (Li *et al*, 2005). In addition, SR (590 nm, 1980 nm) and NDVI (1970 nm, 650 nm) have been used as accurate models to predict LNC (Jia *et al*., 2013b). These prediction models were constructed by correlating hyperspectral reflectance measurements with proven field or lab measurements for the leaf property in question. Multiple linear regression, stepwise regression, support vector machine, machine learning algorithms, and principle component analysis are all common methods for performing this analysis (Li *et al*., 2005, Jia *et al*., 2013b). While the above hyperspectral indices are predictive of LNC under the conditions of each experiment, more research is necessary to test the repeatability of the results with new locations and under different growing conditions.

Since leaf nicotine content is related to chlorophyll content (Howes, 1974), and chlorophyll content is related to changes in reflectance at and around 700 nm (Carter & Knapp, 2001), it is plausible that accurate prediction models for both could be constructed from reflectance measurements. Jia *et al*. (2013a) reported that SR (450 nm, 500 nm) and NDVI (2150 nm, 610 nm) were shown to provide accurate estimates of nicotine content in tobacco. Wei, Liu, and Tang (2018) used hyperspectral ultraviolet reflectance to estimate tobacco leaf nicotine content. Nicotine content is an important factor for tobacco products (Yan, Wang, Qu, & Li, 2001), so a repeatable and accurate model to estimate tobacco leaf nicotine in the field would be advantageous to the tobacco industry.

Pathogen response is another area that can be studied spectrally. Machine learning algorithms have been used to identify wavelengths and/or indices that are able to detect the presence of tobacco mosaic virus (TMV) 48 hours after inoculation, versus five days with the naked eye (Zhu *et al*., 2017). The ability to use a UAV to quickly and non-invasively detect disease levels in tobacco during the incubation period of the pathogen would provide growers the

opportunity to treat pathogen outbreaks before major damage is done or yield is greatly reduced (Zhu *et al*., 2017). More research is needed to validate wavelengths of importance for TMV detection, as well as other important tobacco pathogens.

References

Bhatti, A. U., Mulla, D. J., & Frazier, B. E. (1991) Estimation of soil properties and wheat yields on complex eroded hills using geostatistics and thematic mapper images. *Remote Sensing of Environment, 37*: 181-191.

Birth, G. S., & McVey, G. R. (1968). Measuring the color of growing turf with a reflectance spectrophotometer. *Agronomy Journal, 60*(6): 640-643.

Biswas, D. K., Ma, B. L., & Navabi, A. (2016). Effect of nitrogen rate and fertilizer nitrogen source on physiology, yield, grain quality, and nitrogen use efficiency in corn. *Canadian Journal of Plant Science, 96*(3): 392.

Boegh, E., Soegaard, H., Broge, N., Hasager, C. B., Jensen, N. O., Schelde, K., & Thomsen, A. (2002). Airborne multispectral data for quantifying leaf area index, nitrogen concentration, and photosynthetic efficiency in agriculture. *Remote Sensing of Environment, 81*(2): 179-193.

Bradley, K. W. 2006. A review of the effects of row spacing on weed management in corn and soybean. *Crop Management, 5.*

Brockie, W. (1956). Aircraft in agriculture. *New Zealand Geographer, 12*(1).

Cargill, H. R. (2014). Reconnaissance drones : their first use in the cold war. *Air Power History, 61*(3): 20.

Carter, G. A., & Knapp, A. K. (2001). Leaf optical properties in higher plants: linking spectral characteristics to stress and chlorophyll concentration. *American Journal of Botany, 88*(4): 677-684.

Caturegli, L., Corniglia, M., Gaetani, M., Grossi, N., Magni, S., Migliazzi, M., & Volterrani, M. (2016). Unmanned aerial vehicle to estimate nitrogen status of turfgrasses. *PLoS ONE, 6.*

Christy, C. D. (2008). Real-time measurement of soil attributes using on-the-go near infrared reflectance spectroscopy. *Computers and Electronics in Agriculture, 61*: 10-19.

Clay, D. E., Kim, K. I., Chang, J., Clay, S. A., & Dalsted, K. (2006). Characterizing water and nitrogen stress in corn using remote sensing. *Agronomy Journal, 98*: 579-587.

Corwin, D. L., & Lesch, S. M. (2003). Application of soil electrical conductivity to precision agriculture: theory, principles, and guidelines. *Agronomy Journal, 95*: 455-471.

Duan, T., Chapman, S. C., Guo, Y., & Zheng, B. (2017). Dynamic monitoring of NDVI in wheat agronomy and breeding trials using an unmanned aerial vehicle. *Field Crop Research, 210*: 71-80.

Duarte-Carvajalino, J. M., Alzate, D. F., Ramirez, A. A., Santa-Sepulveda, J. D., Fajardo-Rojas, A. E., & Soto-Suárez, M. (2018). Evaluating late blight severity in potato crops using unmanned aerial vehicles and machine learning algorithms. *Remote Sensing, 10*(10): 1513.

Dupont, J. K., Campenella, R., Seal, M. R., Willers, J. L., & Hood, K. B. (2000). Spatially variable insecticide applications through remote sensing. *Proceedings of the Beltwide Cotton Conference, 2*: 426-429.

Fan, Z., Lu, J., Gong, M., Xie, H., & Goodman, E. (2018). Automatic tobacco plant detection in UAV images via deep neural networks. *IEEE Journal of Selected Topics in Applied Earth Observations and Remote Sensing, Selected Topics in Applied Earth Observations and Remote Sensing, IEEE Journal of, IEEE J. Sel. Top. Appl. Earth Observations Remote Sensing, (3)*: 876.

Gennaro, S. F., Battiston, E., Marco, S. D., Facini, O., Matese, A., nocentini, M., . . . Mugnai, L. (2016). Unmanned aerial vehicle (UAV)-based remote sensing to monitor grapevine leaf

stripe disease within a vineyard affected by esca complex. *Phytopathologia Mediterranea, 2*: 262.

Gitelson, A. A., & Merzlyak, M. N. (1997). Remote estimation of chlorophyll content in higher plant leaves. *International Journal of Remote Sensing, 18*(12): 2691-2697.

Gong, Y., Duan, B., Fang, S., Zhu, R., Wu, X., Ma, Y., & Peng, Y. (2018). Remote estimation of rapeseed yield with unmanned aerial vehicle (UAV) imaging and spectral mixture analysis. *Plant Methods, 1*.

Hock, S. M., Knezevic, S. Z., Martin, A. R., & Lindquist, J. L. (2009). Influence of soybean row width and velvetleaf emergence time on velvetleaf (*Abutilon theophrasti*). *Weed Science, 53*: 160-165.

Honrado, J. L. E., Solpico, D. B., Favila, C. M., Tongson, E., Tangonan, G. L., & Libatique, N. J. C. (2017). UAV imaging with low-cost multispectral imaging system for precision agriculture applications. *IEEE Global Humanitarian Technology Conference (GHTC), San Jose, CA.* p. 1-7.

Howes, C. D. (1974). Nicotine inhibition of carotenoid cyclization in *Cucurbita ficifolia* cotyledons. *Phytochemisty, 13*: 1469-1471.

Jewel, N. (1989). An evaluation of multi-date SPOT data for agriculture and land use mapping in the United Kingdom. *International Journal of Remote Sensing, 10*: 939-951.

Jia, F., Liu, G., Ding, S., Yang, Y., Fu, Y., & Wang, Z. (2013a). Using leaf spectral reflectance to monitor the effects of shading on nicotine content in tobacco leaves. *Industrial Crops & Products, 51*: 444.

Jia, F., Liu, G., Liu, D., Zhang, Y., Fan, W., & Xing, X. (2013b). Comparison of different methods for estimating nitrogen concentration in flue-cured tobacco leaves based on hyperspectral reflectance. *Field Crops Research, 150*: 108-114.

Lamb, D. W., & Brown, R. B. (2001). Remote-sensing and mapping of weeds in crops. *Journal of Agricultural Engineering Research, 78*: 117-125.

Li, F., Liu, L., Wang, J., Li, X., Zhao, C., & Cao, W. (2005). Detection of nitrogen status in FCV tobacco leaves with the spectral reflectance. *Proceedings. 2005 IEEE International Geoscience and Remote Sensing Symposium, 2005. IGARSS '05., Geoscience and Remote Sensing Symposium, 2005. IGARSS '05. Proceedings. 2005 IEEE International, Geoscience and Remote Sensing.* p. 1863.

Li, S., Ding, X., Kuang, Q., Ata-UI-Karim, S. T., Cheng, T., Liu, X., . . . Cao, Q. (2018). Potential of UAV-based active sensing for monitoring rice leaf nitrogen status. *Frontiers in Plant Science, 9*(2018).

Lichtenthaler, H. K. (1996). Non-destructive determination of chlorophyll content of leaves of a green and an aurea mutant of tobacco by reflectance measurements. *Journal of Plant Physiology, 148*: 483-493.

Liu, S., Li, L., Gao, W., Zhang, Y., Liu, Y., Wang, S., & Lu, J. (2018). Diagnosis of nitrogen status in winter oilseed rape (*Brassica napus L.*) using in-situ hyperspectral data and unmanned aerial vehicle (UAV) multispectral images. *Computers & Electronics in Agriculture, 151*: 185-195.

Lowitz, M. (n.d.). The Vegetation Spectrum in Detail. [.jpg]. Retrieved on February 4, 2019 from http://www.markelowitz.com/Hyperspectral.html.

Maxmax. ENDVI. 2015. Retrieved on January 25, 2019 from http://www.maxmax.com/endvi.htm.

Merzlyak, M. N., Gitelson, A. A., Chivkunova, O. B., Solovchenko, A. E., & Pogosyan, S. I. (2003). Application of reflectance spectroscopy for analysis of higher plant pigments. *Russian Journal of Plant Physiology*, *50*(5): 704-710.

Moran, M. S., Inoue, Y., & Barnes, E. M. (1997). Opportunities and limitations for image-based remote sensing in precision crop management. *Remote Sensing of Environment*, *61*: 319-346.

Mulla, D. J. (2013). Twenty five years of remote sensing in precision agriculture: Key advances and remaining knowledge gaps. *Biosystems engineering*, *114*(4).

NASA's Imagine the Universe. (2013). Comparison of wavelength, frequency and energy for the electromagnetic spectrum [.jpg]. Retrieved on January 25, 2019 from Imagehttps://imagine.gsfc.nasa.gov/science/toolbox/emspectrum1.html.

Pinter Jr, P. J., Hatfield, J. L., Schepers, J. S., Barnes, E. M., Moran, M. S., Daughtry, C. S., & Upchurch, D. R. (2003). Remote sensing for crop management. *Photogrammetric Engineering and Remote Sensing*, *69*: 647-664.

Reed, T. D., Johnson, C. S., Wilkinson, C. A., & Barts, S. (2019). 2019 Flue-Cured Tobacco Production Guide. p. 27.

Rouse Jr, J. W., Hass, R. H., Schell, J. A., & Deering, D. W. (1973). Monitoring vegetation systems in the great plains with ERTS. *Proceedings 3rd Earth Resources Technology Satellite (ERTS) symposium, Vol. 1, NASA SP-351, NASA, Washington, DC, USA*. p. 309-317.

Sankaran, S., Quirós, J., Knowles, N., & Knowles, L. (2017). High-resolution aerial imaging based estimation of crop emergence in potatoes. *American Journal of Potato Research, 94*(6): 658.

Shanahan, J. F., Schepers, J. S., Francis, D. D., Varvel, G. E., Wilhelm, W. W., Tringe, J. M., . . . Major, D. J. (2001). Use of remote sensing imagery to estimate corn grain yield. *Agronomy Journal, 93*: 583-589.

Sharma, L. K., Honggang B., Denton, A., & Franzen, D. W. (2015). Active-optical sensors using red NDVI compared to red edge NDVI for prediction of corn grain yield in North Dakota, U.S.A. *Sensors, 15*(11): 27832-27853.

Smith, A. M., Coupland, G., Dolan, L., Harberd, N., Jones, J., Martin, C., . . . Amey, A. (2010). Plant Biology. *Abingdon: Garland Science*.

Sripada, R. P., Heiniger, R. W., White, J. G., & Weisz, R. (2006). Aerial color infrared photography for determining late-season nitrogen requirements in corn. *Agronomy Journal, 97*: 1443-1451.

Svotwa, E., Maasdorp, B., Murwira, A., & Masuka, A. (2012). Selection of optimum vegetative indices for the assessment of tobacco float seedlings response to fertilizer management. *ISRN Agronomy, 2012*: 1-10.

Svotwa, E., Masuka, A. J., Maasdorp, B., & Murwira, A. (2014). Assessing the spectral separability of flue cured tobacco varieties established on different planting dates and under varying fertilizer management levels. *International Journal of Agronomy, 2014*.

Tucker, C. J. (1979). Red and photographic infrared linear combinations for monitoring vegetation. *Remote Sensing of Environment, 8*: 127-150.

Virginia Department of Agriculture and Consumer Services. Virginia's Top 20 Farm Commodities. 2016. Retrieve on May 7, 2019 from https://www.vdacs.virginia.gov/agriculture-top20.shtml

Wei, X. N., Liu, Y., & Tang, Y. L. (2018). Nicotine content of tobacco leaf estimated by UV spectrum. *IOP Conference Series: Earth and Environmental Science, 185*.

What is remote sensing and what is it used for? (n.d.). Retrieved on January 25, 2019 from https://www.usgs.gov/faqs/what-remote-sensing-and-what-it-used?qt-news_science_products=7#qt-news_science_products.

Yan, K. Y., Wang, J. M., Qu, J. B., & Li, X. B. (2001). Correlation between smoking quality and physical/chemical parameters of flue -cured tobacco in Henan Provinc. – Tobacco. *Science & Technology 1*: 5-9.

Zhang, D., Zhou, X., Zhang, J., Lan, Y., Xu, C., & Liang, D. (2018). Detection of rice sheath blight using an unmanned aerial system with high-resolution color and multispectral imaging. *PLoS ONE, 13*(5): 1-14.

Zhang, X., Friedl, M., Schaaf, A., Strahler, C. B., Hodges, A. H., Gao, J. C. F., . . . Huete, B. C. A. (2003). Monitoring vegetation phenology using MODIS. *Remote Sensing of Environment, 84*: 471-475.

Zhao, B., Zhang, J., Yang, C., Zhou, G., Ding, Y., Shi, Y., . . . Liao, Q. (2018). Rapeseed seedling stand counting and seeding performance evaluation at two early growth stages based on unmanned aerial vehicle imagery. *Frontiers in Plant Science, 9*(2018).

Zhu, H., Chu, B., Zhang, C., Liu, F., Jiang, L., & He, Y. (2017). Hyperspectral imaging for presymptomatic detection of tobacco disease with successive projections algorithm and machine-learning classifiers. *Scientific Reports (Nature Publisher Group), 7*: 1.

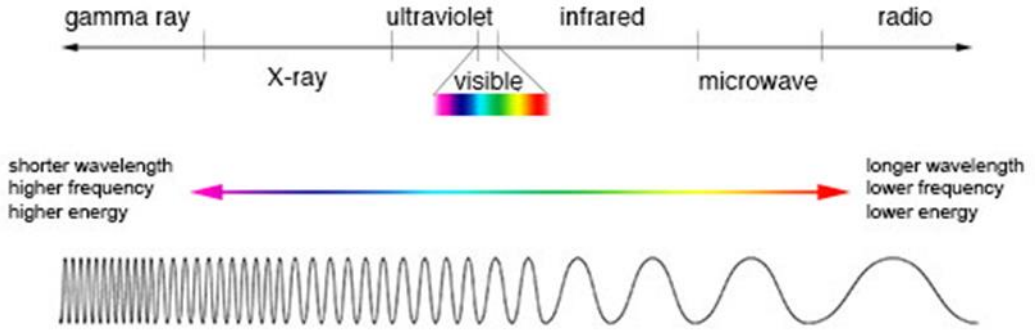

Figure 2.1- Electromagnetic spectrum (NASA 2013)

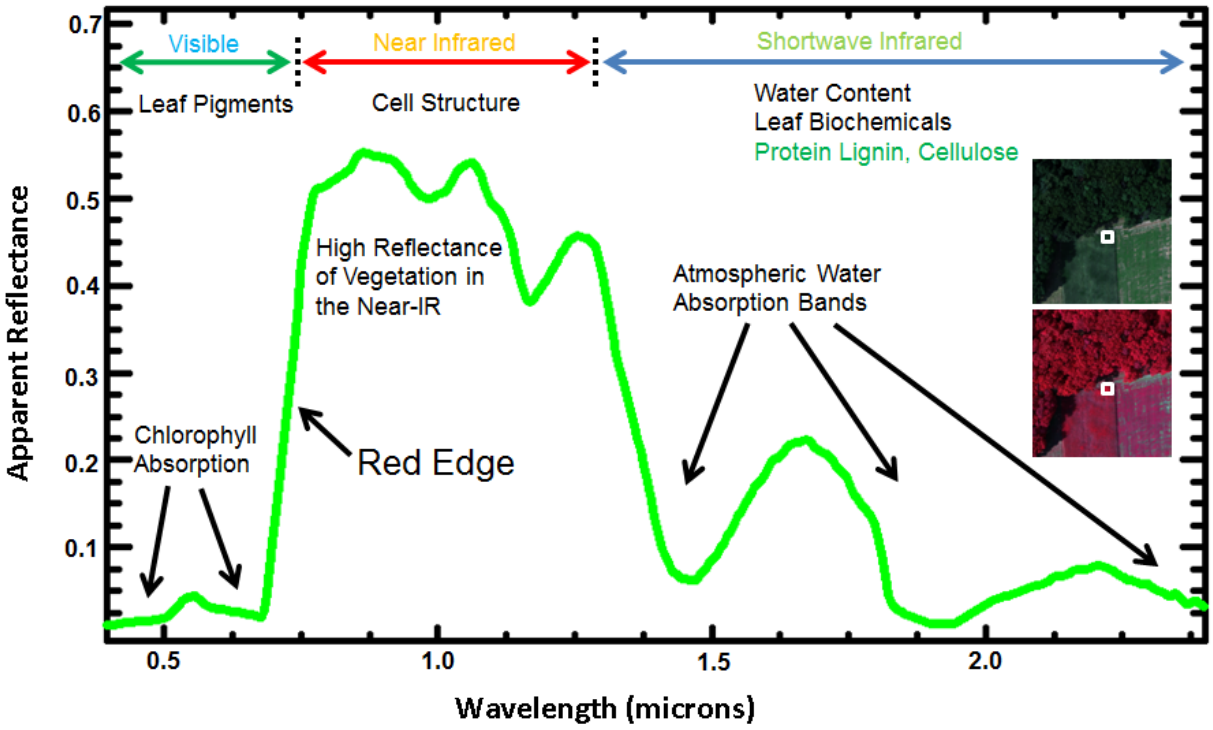

Figure 2.2- Reflectance profile of vegetation (Lowitz n.d.)

Chapter III

Varietal and Nitrogen Rate Response of Flue-Cured Tobacco Using Aerial Assessment

Introduction

Flue-cured tobacco is a high value crop that is intensively managed to achieve maximum yield and quality. Nitrogen rate and variety selection are important factors in achieving a profitable yield of high quality tobacco. Traditional scouting methods involve walking fields on foot and making management decisions based on visual observation. UAVs have potential to rapidly assess flue-cured tobacco, which may assist growers and researchers in decision making and be useful in a precision management strategy.

Nutrient management is one of the key factors that contributes to the yield and quality of flue-cured tobacco. Nutrient levels can have a major effect on tobacco leaf chemistry (Su *et al*., 2006), which is a component of quality. Of all the nutrients that must be managed for a flue-cured tobacco crop, nitrogen is perhaps the most significant. Nitrogen is one of the main building blocks for chlorophyll in plants. Without sufficient chlorophyll production, photosynthetic rates are reduced and plants lack the energy production needed to maximizing yield.

Ample available nitrogen is paramount for flue-cured tobacco from the seedling stage through the removal of terminal inflorescence, in order to achieve maximum leaf quality and yield. During this early season stage, nitrogen is needed to promote rapid accumulation of biomass. Studies indicate that nitrate levels during this period are directly related to final leaf yield and quality (MacKown *et al*., 2000). While most crops require a sufficient quantity of nitrogen for proper growth, flue-cured tobacco is sensitive to over-fertilization of nitrogen (Yang

et al., 2011). In order to achieve desired cured leaf quality, flue-cured tobacco must progress through leaf maturation followed by ripening. The initiation of this leaf ripening is due, in large part, to the depletion of soil available nitrogen (Yang *et al*., 2011). Therefore, if nitrogen is over-applied, this can lead to a delay in ripening.

Variety selection also plays a large role in maturation and ripening of flue-cured tobacco. Varieties are available with differing maturation dates and levels of disease resistance. Early-maturing flue-cured tobacco varieties ripen earlier in the growing season compared to late-maturing varieties. This makes management timing different, depending on the maturation date of a given variety.

Vegetation indices use reflectance values over given ranges or bands of the electromagnetic spectrum to calculate values that have a relationship to a vegetation parameter of interest. Commonly used bands for vegetation indices include blue (452 -512 nm), green (533 - 590 nm), red (636 - 673 nm), and near-infrared or NIR (851 - 879 nm) (Barsi *et al*. 2014). The normalized difference vegetation index (NDVI) is the most common vegetation index used in plant science. The formula (Rouse, 1973) for which is below:

$$Normalized\ Difference\ Vegetation\ Index = \frac{NIR - Red}{NIR + Red}$$

NDVI is used as a predictor of overall plant health and vigor and is influenced by leaf chlorophyll content (Boegh *et al*., 2002). NDVI has been shown to be predictive of nitrogen content of tobacco seedlings (Svotwa, Maasdorp, Murwira, & Masuka, 2012) and was also shown to have vary with flue-cured tobacco nitrogen rates, as well as varieties, once leaf ripening had begun and chlorophyll levels were reduced (Svotwa, Masuka, Maasdorp, & Murwira, 2014). NDVI was shown to be significantly lower for early maturing varieties and low

rates of nitrogen, compared to late maturing varieties and higher nitrogen rates during the late season (Svotwa *et al*., 2014). The enhanced normalized difference vegetation index (ENDVI) is a variation of NDVI that uses the blue and green bands of light instead of red and is optimized for low altitude aerial imagery, such as UAV-acquired imagery.

Research regarding the use of ENDVI to determine between flue-cured tobacco varieties and nitrogen fertilization levels is limited. A two-year study was conducted near Blackstone, VA at the Virginia Tech Southern Piedmont Agricultural Research and Extension Center to evaluate the use of aerial ENDVI surveys for this purpose. The objectives of this study were:

1. Observe the seasonal patterns in ENDVI for a flue-cured tobacco crop and investigate ENDVI response to crop management events.
2. Evaluate the differences in ENDVI values in relation to nitrogen fertilization rate and variety.

Materials and Methods

Aerial surveys were conducted over a variety X N-rate test at the Southern Piedmont Agricultural Research and Extension Center near Blackstone, VA during the 2017 and 2018 growing seasons. Ten varieties in 2017 and nine varieties in 2018 (Table 3.1) were treated with three N-rate treatments in a split-plot design with four replications. Nitrogen was applied in two applications for both years: once before transplanting, and once approximately 20 days after transplanting (DAT). For 2017, the three N-rates were 55 lbs/ac, 75 lbs/ac, and 100 lbs/ac. The 2018 N-rates were 60 lbs/ac, 80 lbs/ac, and 100 lbs/ac (Table 3.1). The differences in varieties and N-rates between years is due the observation area being part of a separate study. Four varieties which were included in both years were chosen for analysis. During 2017, twenty aerial

surveys were made from 36 to 125 DAT and eight aerial surveys were taken in 2018 from 34 to 127 DAT. The reduction in survey quantity in 2018 was an attempt to reduce the time spent on imagery collection and post-processing. Flights were made using a DJI Matrice 100 quadcopter (SZ DJI Technology Co., Ltd., Shenzhen, China) and a DJI Zenmuse X3 camera (SZ DJI Technology Co., Ltd., Shenzhen, China) with a BGNIR (blue, green, NIR) multispectral lens (Figure 3.1). The spectral response of the Zenmuse X3 camera is shown in Fig. 3.2. The light radiance over these ranges was used in calculation of vegetation indices. Flights were made under full sunlight conditions in 2017 but were made under cloud cover the second year, in order to evaluate performance under both conditions. Survey flights were made at no greater than one hour from solar noon in both years.

Automated flight paths were set to capture aerial images of the field plots with a 70% overlap (horizontal and vertical) at an altitude of approximately 50 meters above ground level. This provided a pixel resolution of 2.5 cm^2. The images were stitched together into a whole field orthomosaic using PrecisionMapper™ software (PrecisionHawk, Raleigh, NC) and ENDVI was calculated for all orthomosaics using the equation below ("Maxmax", 2015).

$$Enhanced\ Normalized\ Difference\ Vegetation\ Index = \frac{(NIR + Green) - (2 \times Blue)}{(NIR + Green) + (2 \times Blue)}$$

Zonal statistics were calculated with ESRI (Redlands, CA) ArcGIS software to extract the mean ENDVI values of each plot for each observation date (Fig. 3.3). Mean ENDVI values of N-rates, varieties, and years were analyzed for variance using PROC T-test in SAS statistical software (SAS Institute, Cary, NC) and corresponding graphs plotted using SigmaPlot 12.3 (Systat Software, Inc., San Jose, CA). Means were pooled and treatments separated when appropriate.

Results and Discussion

Seasonal Crop Development Assessment with ENDVI

The seasonal ENDVI graph of the flue-cured tobacco in 2017 suggest three phases approximating the developmental stages of the crop: (1) rapid plant growth, (2) leaf expansion and dry weight accumulation, and (3) leaf maturation and ripening (Fig. 3.4). The first observation was made near layby, at 35 DAT. Layby is the last cultivation of a tobacco crop, where soil is moved around the base of the plant to create a high raised row ridge. ENDVI values increased with each observation date from 35 to 67 DAT. The crop was topped (removal of terminal inflorescence) at 65 DAT. Topping prevents reproductive growth and enhances leaf expansion. From 67 to 81 DAT, ENDVI decreased as the tobacco began to ripen. Variance in sunlight irradiance may have been the cause for increased values from 85 to 93 DAT. Values from 95 to 125 DAT plateau, remaining near 0.36 for the remainder of the observation period. During this period, the crop was nearing full ripeness and harvest of the lower leaves had begun. Observation of these three phases is supported by the slope of the linear line segment for each phase.

Trends were generally similar between the overall seasonal ENDVI graph for 2018 (Fig. 3.5) and that for 2017. The slopes of the line segments for the three phases observed in 2018 approximate those observed in 2017. However, the ENDVI values were consistently lower throughout the 2018 season when compared to the ENDVI values for 2017. The overall ENDVI mean of all observations dates was 0.4172 in 2017 and 0.2026 in 2018. This is most likely due to the differing cloud cover during the flights. Souza, Scharf, and Sudduth (2010) highlighted the effects that cloud cover has on NDVI. They found that shading can cause significant reduction in NDVI values. The 2018 growing season had an extremely high amount of rainfall (Table 3.2),

which may have also contributed to the decline in overall ENDVI in 2018. From 34 to 61 DAT, ENDVI increased in 2018. The 2018 crop was topped at 63 DAT, and values decreased from 61 to 127 DAT.

There was a significant correlation between the total integrated area under the ENDVI curve, or area under vegetation index curve (AUVI), and the yield of the plots for both 2017 ($r = 0.49$, $p < 0.0001$) and 2018 ($r = 0.60$, $p < 0.0001$). The correlation of these variables is reasonably high, given the number of other factors that affect yield. This correlation demonstrates the potential of aerial ENDVI imagery to be used as a yield predictor in flue-cured tobacco. The use of ENDVI to predict flue-cured tobacco yield would be a beneficial application for producers.

Varietal Influence on ENDVI

Four varieties were chosen for statistical analysis based on their maturity class: PVH 2310, PVH 2254, K 326, and NC 196. The latter two are widely grown and are late maturing varieties. PVH 2310 is an early maturing and PVH 2254 is a late maturing variety which tends to ripen to a greener color when compared to similar varieties. Results of ANOVA for the 2017 data indicate a significant variety effect ($p < 0.0001$). The interaction of variety and N-rate was not significant ($p = 0.6211$). PVH 2254 and PVH 2310 exhibited the highest and lowest ENDVI values in the late stages of the 2017 growing season, respectively (Fig. 3.6). NC 196 frequently had the lowest ENDVI in the early season, before topping. At 89 DAT and after, the ENDVI of the varieties had a significant positive relationship to maturity date based on mean separation. Significant differences among the varieties were observed in the area under vegetation index (AUVI) after topping (65 DAT), as nitrogen was depleted from the soil and the tobacco began to mature and ripen (Table 3.3). The relationship between ENDVI and variety maturation date is consistent with the NDVI data presented in Svotwa *et al*. (2014). In 2018, the data follow a

similar trend, with respect to varietal maturity, as seen in 2017 (Fig. 3.7). Results of ANOVA for the 2018 data indicate a significant variety effect ($p = 0.0391$). The interaction of variety and N-rate was not significant ($p = 0.9624$). PVH 2254 had significantly higher mean ENDVI values at the last three observation dates. Beyond 67 DAT, PVH 2310 was the variety with the lowest mean ENDVI, as seen in 2017. However, mean ENDVI for PVH 2310 was relatively high at and before topping (63 DAT). Significant differences in the AUVI of the varieties were observed from first harvest to the final crop survey (Table 3.3). Separation in mean ENDVI among these four varieties increased over time during both years. This would be expected, as varietal difference would manifest as the leaves mature and prior to harvest.

Nitrogen influence on ENDVI

Results of ANOVA for the 2017 data indicate a significant N-rate effect ($p < 0.0001$). The interaction of variety and N-rate was not significant ($p = 0.6211$). Mean ENDVI for N-rates was separable based on mean separation after topping in 2017 (Fig. 3.8). Although at 89 DAT the differences in the mean ENDVI was not significant for N-rates, the trend was consistent with the rest of the late-season surveys. After topping (65 DAT), ENDVI showed separation of the N-rates based on mean separation, with the 55 lbs/ac N-rate exhibiting the lowest mean ENDVI and the high N-rate exhibiting the highest ENDVI. However, this trend was not observed in the early season. Similarly, the AUVI was not significant, with respect to N-rate, from transplanting to topping but significant differences were observed from topping to final crop survey (Table 3.4). This is to be expected since available nitrogen should not be a limiting factor in the early season under these N-rates (Yang *et al*., 2011). Results of ANOVA for the 2018 data indicate a significant N-rate effect ($p < 0.0001$). The interaction of variety and N-rate was not significant ($p = 0.9624$). In 2018, separation in ENDVI was also observed with respect to N-rate (Fig. 3.9).

Mean ENDVI was separable, based on nitrogen rate from 34 DAT to 99 DAT. However, in contrast to the data from 2017, this relationship did not continue. For the last 2 observation dates, ENDVI values were not significant and the 60 lbs/ac N-rate treatment had a higher mean ENDVI than the 80 lbs/ac N-rate treatment for the last three observations. Given the high amount of early season rainfall in the 2018 growing season (Table 3.2), there is a possibility that leaching of nitrogen below the crop rooting zone impacted the typical depletion of nitrogen. Similarly, although nitrogen is not generally a limiting factor for flue-cured tobacco in the early season, above normal amounts of rainfall in the early season may have resulted in some degree of nitrogen leaching and perhaps reduced root system development in the 2018 growing season (Table 3.2). This could be the cause for the significant differences in the AUVI of the N-rate treatments in the early season, from transplanting to topping (Table 3.4) as well as the mean separation observed as early as 34 DAT (Fig. 3.9).

Conclusions

The results of this study are similar to the findings of Svotwa *et al*. (2014), who used NDVI rather than the ENDVI surveys used in this study. In both studies, significant varietal differences did not appear until the middle of the growing season, around topping. However, in 2018, a significant ENDVI response to nitrogen application rates occurred earlier than observed in Svotwa *et al*. (2014). This could be attributed to nitrogen leaching through the soil profile, due to heavy rainfall in the early season of 2018, which depleted the soil of available nitrogen sooner than normal.

Aerial ENDVI surveys showed the ability to consistently differentiate both varieties and N-rates at and after topping. Further research is needed to address the efficiency of using ENDVI surveys to facilitate precision application of inputs, such as nitrogen application, in flue-cured

tobacco. However, ENDVI does show a positive relationship to nitrogen fertilization rate. The challenge with this problem is having significant differences between nitrogen levels early enough for layby fertilization. In 2017, significant differences in ENDVI, based on N-rate, did not occur until topping. This is logical, given that the tobacco starts to deplete the soil of available nitrogen at this time (Yang *et al*., 2011). However, topping occurs beyond the stage which nitrogen is typically applied to flue-cured tobacco. If ENDVI is to be used to facilitate precision application of nitrogen, differences in ENDVI, with respect to nitrogen, must be present early enough to act on. The lack of significance in ENDVI values for N-rate in 2017 may indicate that remedial application of nitrogen was unnecessary in that growing season. In 2018, heavy early season rainfall may have led to the significant difference in N-rate at layby. In this year, ENDVI differences based on nitrogen did appear early enough to be used in nitrogen application decisions. Based on these results, future studies should be implemented to evaluate the ability of ENDVI to be used as a prediction of leaf nitrogen content as well as set ENDVI thresholds for leaching adjustments.

ENDVI correlations to crop yield, presented in this study, exhibit the potential of aerial remote sensing to be used for flue-cured tobacco yield predictions. Knowledge regarding yield expectancy would be advantageous to tobacco producers by assisting in planning of curing schedules and identifying low-yielding areas of fields that could be improved. Further research is necessary to determine the viability of using aerial ENDVI surveys for yield prediction. However, the results presented show that such research is warranted.

The large differences seen between the ENDVI in 2017 and 2018 highlight the importance of radiometric correction. Radiometric correction allows for temporal measurements to be compared accurately by using radiometric calibration panels placed in the survey area or a

sunlight irradiance sensor mounted on top of the UAV to normalize surveys based on sunlight irradiance. Radiometric correction was not applied to the imagery in this study. The differences in the overall ENDVI mean between the two years illustrate that ENDVI can be heavily influenced by sunlight irradiance. The surveys taken in 2018, with full cloud cover, have much lower ENDVI values when compared to surveys taken in 2017 under full sunlight. When using aerial imaging to make comparisons over time, radiometric correction is necessary to minimize the effects of changes in sunlight irradiance.

References

Barsi, J.A., Lee, K., Kvaran, G., Markham, B.L., Pedelty, J.A. (2014). The spectral response of the landsat-8 operational land imager. *Remote Sensing, 6*: 10232-10251.

Boegh, E., Soegaard, H., Broge, N., Hasager, C. B., Jensen, N. O., Schelde, K., & Thomsen, A. (2002). Airborne multispectral data for quantifying leaf area index, nitrogen concentration, and photosynthetic efficiency in agriculture. *Remote Sensing of Environment, 81*(2): 179-193.

MacKown, C.T., Crafts-Brandner, S.J., & Sutton, T.G. (2000). Early-season plant nitrate test for leaf yield and nitrate concentration of air-cured burley tobacco. *Crop Science, 40*(1): 165-170.

Maxmax. ENDVI. 2015. Retrieved on January 25, 2019 from http://www.maxmax.com/endvi.htm.

Rouse Jr, J. W., Hass, R. H., Schell, J. A., & Deering, D. W. (1973). Monitoring vegetation systems in the great plains with ERTS. *Proceedings 3rd Earth Resources Technology Satellite (ERTS) symposium, Vol. 1, NASA SP-351, NASA, Washington, DC, USA*: 309-317.

Souza, E.G., Scharf, P.C., & Sudduth, K.A. (2010). Sun position and cloud effects on reflectance and vegetation indices of corn. *Agronomy Journal 102*: 734-744.

Su, F., Fu, L., Chen, H., & Hong, L. (2006). Balancing nutrient use for flue-cured tobacco. *Better Crops, 90*(4): 23-25.

Svotwa, E., Maasdorp, B., Murwira, A., & Masuka, A. (2012). Selection of optimum vegetative indices for the assessment of tobacco float seedlings response to fertilizer management. *ISRN Agronomy, 2012*: 1-10.

Svotwa, E., Masuka, A. J., Maasdorp, B., & Murwira, A. (2014). Assessing the spectral separability of flue cured tobacco varieties established on different planting dates and under varying fertilizer management levels. *International Journal of Agronomy, 2014*.

Yang, Z.X., Liu, H.B., Ke, Y.S., Wu, W.B., Zhang, X.Q., Qiu, M.W., … Yang, T.-Z. (2011). Nitrogen uptake and allocation characteristics of flue-cured tobacco in Nanxiong tobacco-planting area of Guangdong Province. *The Journal of Applied Ecology, 22*(6): 1450-1456.

Table 3.1- Variety and nitrogen rate treatments evaluated in the field trial from which UAV flights and subsequent analyses were conducted in 2017 and 2018 at the Virginia Tech Southern Piedmont Center near Blackstone, VA.

2017		**2018**	
Varieties	**Nitrogen Rates**	**Varieties**	**Nitrogen Rates**
K 326	55 lbs/ac	*K 326*	60 lbs/ac
NC 196	75 lbs/ac	*NC 196*	80 lbs/ac
PVH 2254	100 lbs/ac	*PVH 2254*	100 lbs/ac
PVH 2310		*PVH 2310*	
PVH 1118		PVH 1452	
PVH 1452		PVH 1600	
PVH 1600		PVH 1920	
PVH 1920		PVH 2110	
PVH 2110		PVH 2275	
K 326 Pylw			

Figure 3.1- Matrice 100 quadcopter with Zenmuse X3 BGNIR camera being flown over the study area in the mid-season after topping has taken place. Flights were made at 50 meters above ground level.

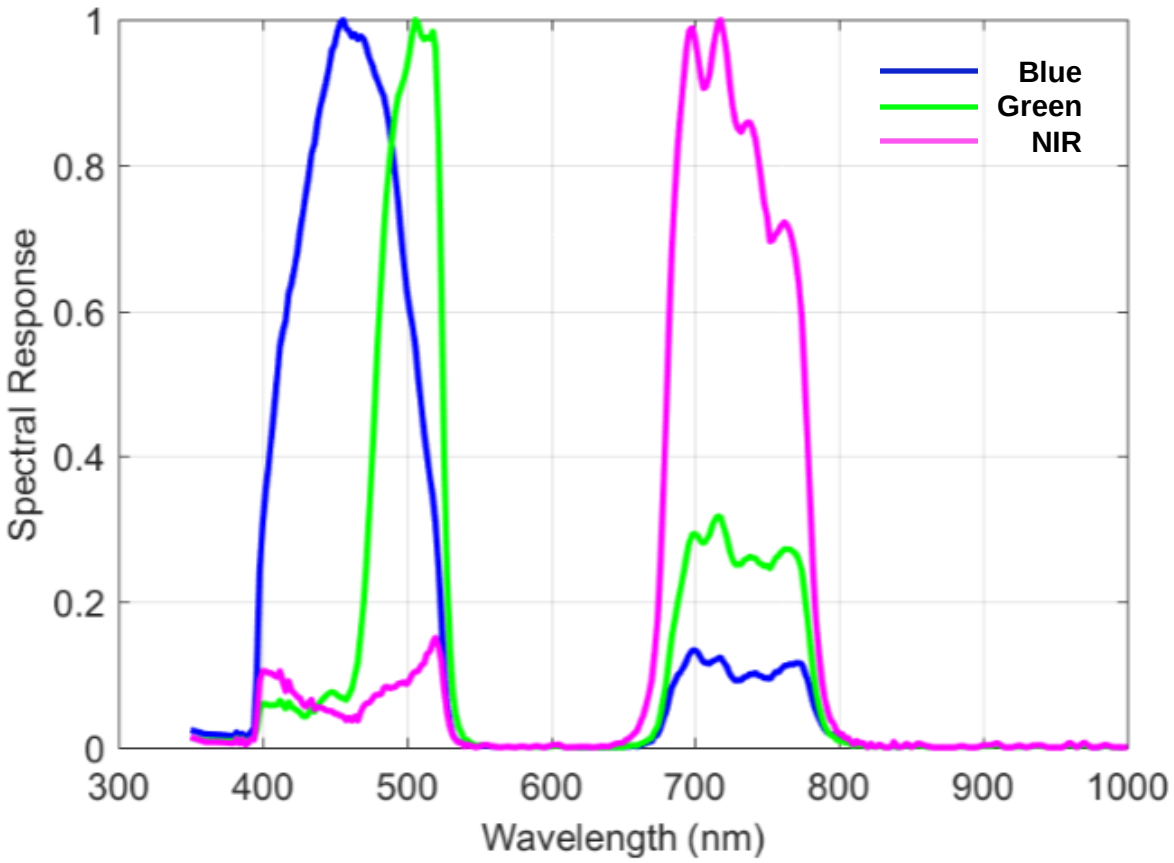

Figure 3.2- Spectral response of Zenmuse X3 BGNIR camera used for aerial surveys shows the wavelengths used for input into the ENDVI equation used in the study (PrecisionHawk, Raleigh, NC).

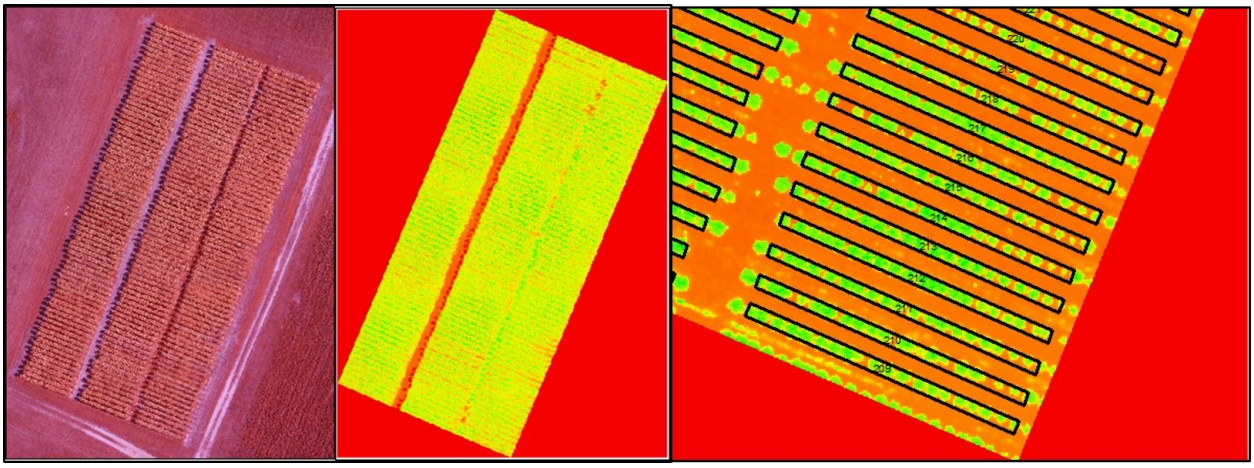

Figure 3.3- BGNIR orthomosaic surveys were taken of the study area (left) and ENDVI was applied (center). Zonal statistics were used to compute mean ENDVI values for single-row plots (right).

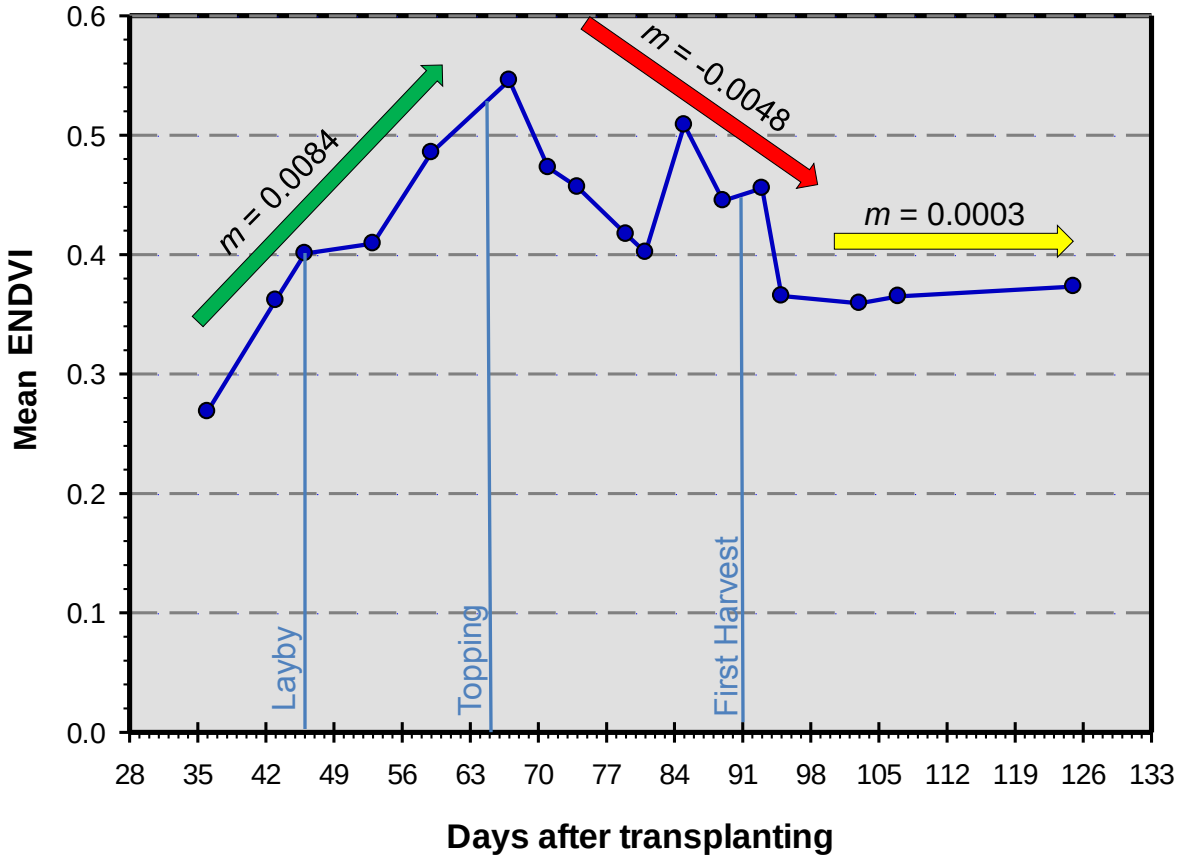

Figure 3.4- Seasonal pattern in ENDVI combined over varieties and N-rates in 2017. Three growth phases can be observed corresponding to: rapid plant growth (green arrow), leaf expansion and dry weight accumulation (red arrow), and leaf maturation and ripening (yellow arrow). Topping occurred at 65 DAT, coinciding with peak ENDVI of the crop. Slopes (*m*) of linear regressions at each phase are included.

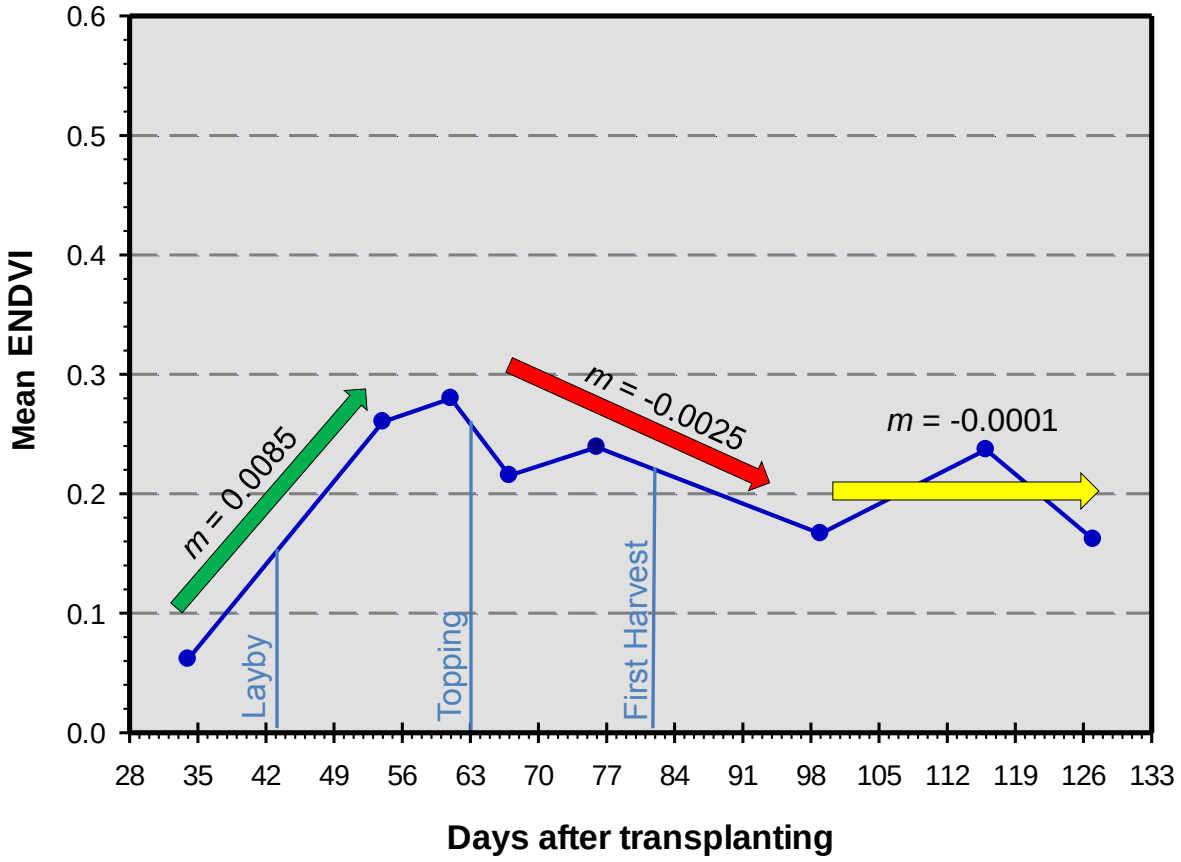

Figure 3.5- Seasonal pattern in ENDVI combined over varieties and N-rates in 2018. Topping occurred at 63 DAT which was just after the peak ENDVI at 61 DAT. The 2018 flights were made with the presence of cloud cover. Slopes (*m*) of linear regressions at each phase are included.

Table 3.2- Comparative rainfall amounts (inches) occurring on flue-cured tobacco crops at the Southern Piedmont Center in 2017 and 2018.

	Rainfall (in)	
	2017	**2018**
Transplanting - Layby	6.6	12.7
Layby - Topping	2.9	3.0
Topping - Last Survey	9.4	11.1
Total	18.8	26.7

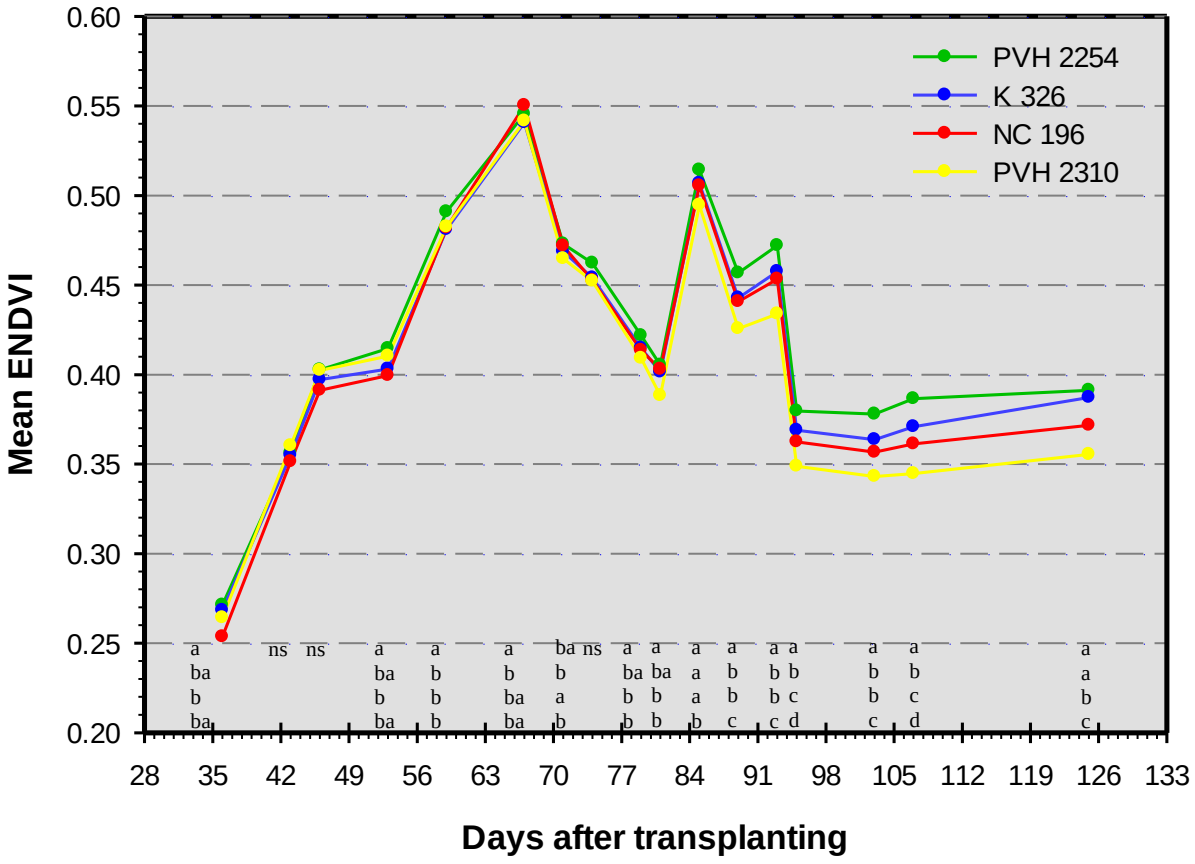

Figure 3.6- Seasonal pattern of ENDVI for four flue-cured tobacco varieties combined over three nitrogen rates in 2017. Mean separation letters for LSD (*alpha* = 0.05) are arranged in the same order as the legend.

Table 3.3- Mean area under vegetation index curve (AUVI) for four flue-cured tobacco varieties in 2017 and 2018. A season total is shown, as well as the position of the curve corresponding to three phases of crop development (transplanting to topping, topping the first harvest, and first harvest to final crop survey. Means followed by the same letter are not significantly different (LSD *alpha* = 0.05) within the same year.

		AUVI			
	VARIETY	**Season Total**	**Phase 1**	**Phase 2**	**Phase 3**
2017					
	PVH 2254	37.47 a	13.05	12.04 a	12.37 a
	K 326	36.80 b	12.85	11.91 a	12.05 b
	NC 196	36.40 b	12.77	11.91 a	11.72 c
	PVH 2310	35.67 c	12.95	11.50 b	11.23 d
	p-value	<0.0001	ns	0.007	<0.0001
2018					
	PVH 2254	8.51 a	2.02	3.22	3.27 a
	K 326	7.92 b	1.84	3.03	3.05 b
	NC 196	7.86 b	1.88	3.03	2.94 b
	PVH 2310	7.82 b	1.99	3.08	2.75 c
	p-value	0.0116	ns	ns	<0.0001

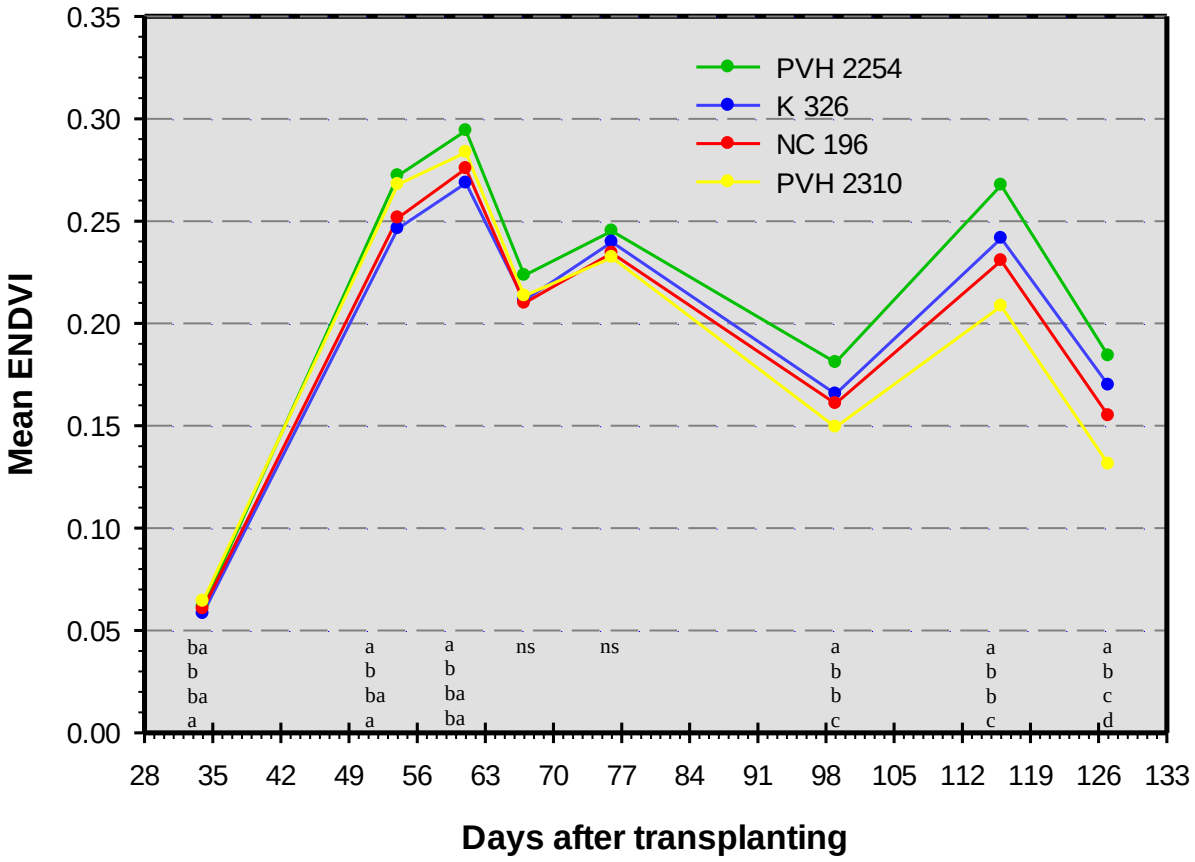

Figure 3.7- Seasonal pattern of ENDVI for four flue-cured tobacco varieties combined over three nitrogen rates in 2018. Mean separation letters for LSD (*alpha* = 0.05) are arranged in the same order as the legend.

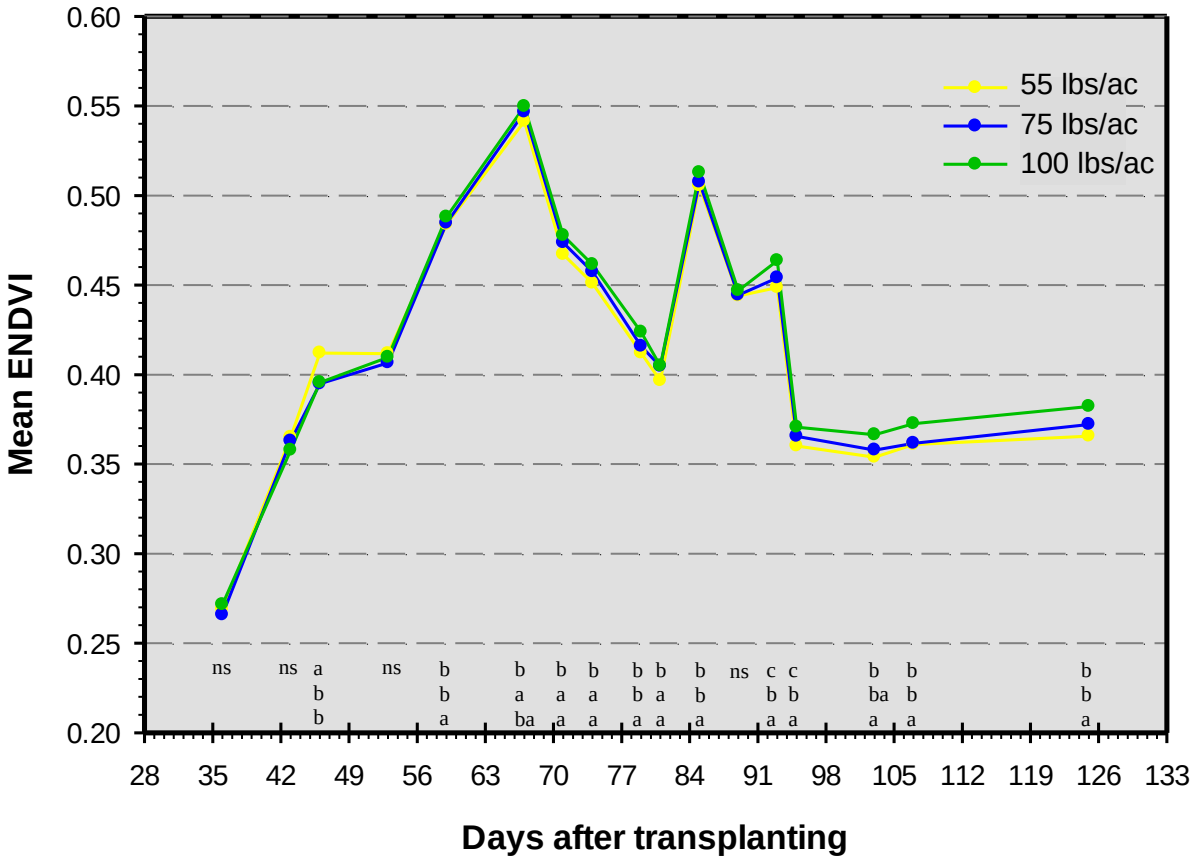

Figure 3.8- Seasonal pattern of ENDVI for three nitrogen rates combined over ten flue-cured tobacco varieties in 2017. Mean separation letters for LSD (*alpha* = 0.05) are arranged in the same order as the legend.

Table 3.4- Mean area under vegetation index curve (AUVI) for three nitrogen rates in 2017 and 2018. A season total is shown, as well as the position of the curve corresponding to three phases of crop development (transplanting to topping, topping the first harvest, and first harvest to final crop survey. Means followed by the same letter are not significantly different (LSD *alpha* = 0.05) within the same year.

		AUVI			
	N-rate	**Season Total**	**Phase 1**	**Phase 2**	**Phase 3**
2017					
	55 lbs/ac	36.31 b	13.05	11.65 b	11.61 b
	75 lbs/ac	36.66 b	12.94	11.97 a	11.76 b
	100 lbs/ac	37.08 a	12.99	12.03 a	12.05 a
	p-value	0.0002	ns	0.0004	<0.0001
2018					
	60 lbs/ac	7.74 b	1.82 b	2.94 b	2.98 b
	80 lbs/ac	8.13 a	2.00 a	3.14 a	2.99 b
	100 lbs/ac	8.30 a	1.99 a	3.20 a	3.11 a
	p-value	<0.0001	<0.0001	<0.0001	0.0112

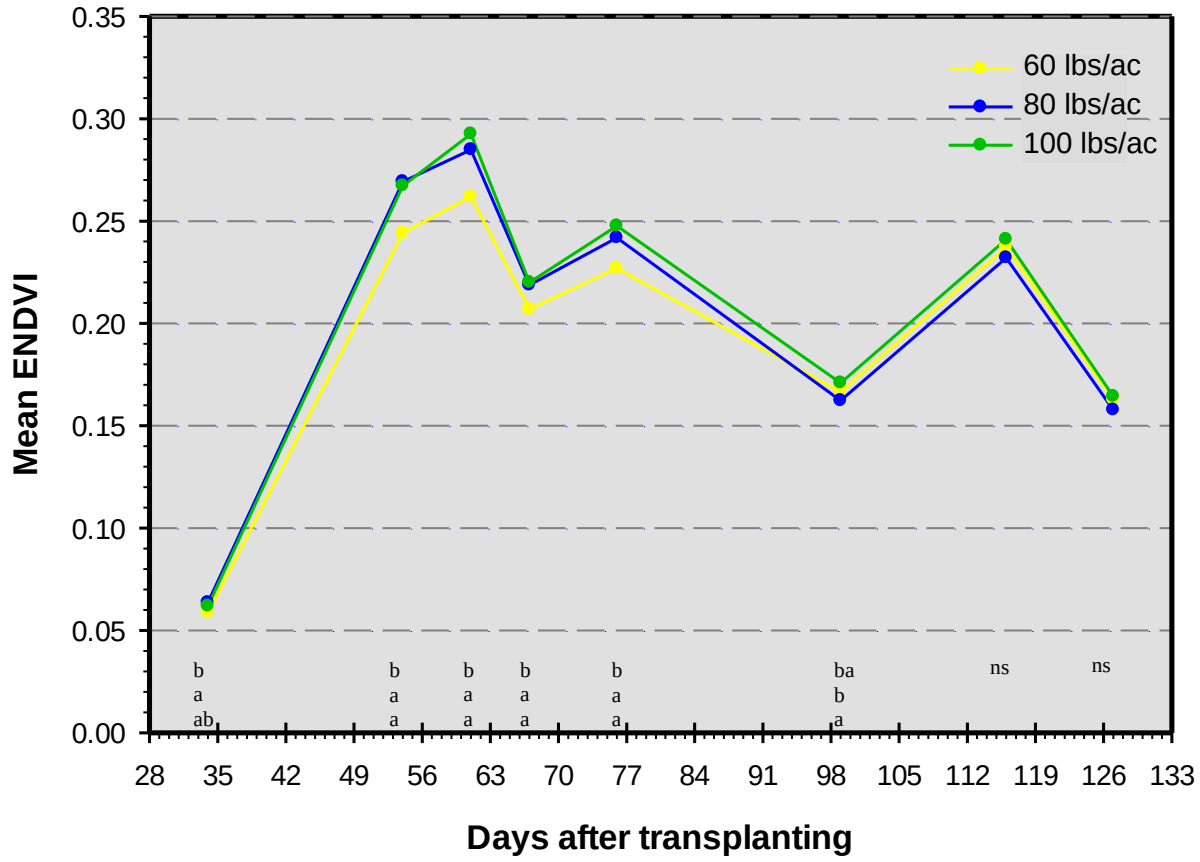

Figure 3.9- Seasonal pattern of ENDVI for three nitrogen rates combined over nine flue-cured tobacco varieties in 2018. Mean separation letters for LSD (*alpha* = 0.05) are arranged in the same order as the legend.

Chapter IV

Hyperspectral Index Development for Detection of Black Shank Incidence in Flue-Cured Tobacco

Introduction

The most important component determining the usefulness of an unmanned aerial vehicle (UAV) to remotely analyze crops is the camera or sensor deployed. The sensor(s) carried by the UAV determines the data type and quality measured. The most common sensors are spectral cameras, but others may include light detection and ranging (LiDAR), thermal, and radar. In their most basic form, spectral cameras digitally record data using three bands of visible light: blue, green, and red. Hence, these are often referred to as visible range cameras. These cameras render an image by calculating a value for each band of visible light for each pixel in a frame. Near-infrared (NIR) cameras work in a similar manner as visible range cameras, but measure light intensity in the NIR range of light (750 - 1400 nm) beyond the range that the human eye can detect. The use of a NIR camera is necessary for calculation of the normalized difference vegetation index (NDVI) as well as many other NIR vegetation indices.

Visual range and NIR cameras having 3 to 10 bands are commonly referred to as multispectral cameras. Hyperspectral cameras have a higher spectral resolution than multispectral cameras and measure hundreds of very narrow bands that range from 1 - 30 nm on the electromagnetic spectrum (GISGeography, 2018). Hyperspectral cameras store data as a 3-D matrix, with the x and y planes consisting of pixels representing the target surface (like a normal image) and the z plane consisting of a stack of those images, each representing a narrow wavelength range (Figure 4.1). Hyperspectral point measurement sensors, such as

spectroradiometers, could be equated to one pixel of a hyperspectral image (Figure 4.1). These sensors render a spectral profile, or spectral signature, of a target surface with the electromagnetic spectrum as the x-axis and electromagnetic energy on the y-axis.

Hyperspectral data have a higher resolution when compared with multispectral data, and are better suited to predicting specific plant properties (Jia *et al*., 2013a; Jia *et al*., 2013b). Zhu *et al*. (2017) used hyperspectral imaging to detect tobacco mosaic virus (TMV) pre-symptomatically. Ground-based hyperspectral data have been used to detect specific disease incidence of tomato spotted wilt virus (TSWV) in capsicum plants (Moghadam *et al*., 2017), peanut leaf spot in peanuts (Chen, Zhang, Chen, Wan, & Zhang, 2019), yellow leaf curl in tomatoes (Lu, Zhou, Gao, & Jiang, 2018), and charcoal rot disease in soybeans (Nagasubramanian *et al*., 2018).

Phytophthora nicotianae (black shank) is a soilborne fungus like pathogen of tobacco. Common symptoms are chlorosis, wilting of the leaves, stalk rot, and eventual plant death (Daub *et al*., 1990). Black shank is one of the most common and detrimental pathogens of flue-cured tobacco crops in Virginia. If left untreated, black shank infestations can cause 100% loss in some fields (Daub *et al*., 1990).

Hyperspectral data have the potential to be a powerful tool for disease detection of plants (Mahlein, Oerke, Steiner, & Dehne, 2012). Therefore, a field study was conducted in a commercial field with a black shank infestation to evaluate the use of hyperspectral data to detect black shank incidence in flue-cured tobacco. The objectives of this study were:

1. Observe differences in the mean spectral profiles of black shank symptomatic plants and asymptomatic plants.

2. Investigate the potential of developing a hyperspectral index to detect black shank incidence before quality and yield is significantly reduced.
3. Determine specificity of the hyperspectral index to black shank detection by testing the proposed index on *Ralstonia solanacearum* (Granville wilt) symptomatic and asymptomatic plants.
4. Test the ability of machine learning algorithms to predict symptomatic and asymptomatic plants and compare the accuracy of machine learning algorithms to the proposed hyperspectral index.

Materials and Methods

A commercial flue-cured tobacco production field near Union Level, VA with a quickly spreading black shank infestation was observed during the 2018 growing season. An observation area of 40 consecutive plants was selected. The area was chosen because of the equal distribution of black shank symptoms in the area. At the inception of the experiment, approximately half of the plants in the observation area displayed varying levels of disease symptoms and half appeared healthy.

Hyperspectral reflectance spectra were measured using an SR-3500 (Spectral Evolution, Lawrence, MA) full range (350 - 2500 nm) spectroradiometer. The spectral resolution of the SR-3500 is 3 nm at 700 nm, 8 nm at 1500 nm, and 6 nm at 2100 nm. The spectroradiometer was used with a leaf-clip attachment in order to minimize atmospheric effects. Measurements of each plant in the observation area were taken on four dates: Aug. 2, 9, 13, and 17. This was after terminal inflorescence had been removed and directly prior to harvest. Measurements were taken from the 3rd leaf from the top of each plant between the 6th and 7th lateral vein from the base of

the leaf. At all observation dates, a visual health rating was recorded as asymptomatic, symptomatic, or diseased for each plant in the observation area (Figure 4.2). Plants rated as asymptomatic exhibited no visual disease symptoms. Symptomatic plants had early visual symptoms of black shank, such as yellowing and wilting of lower leaves. Diseased-rated plants had developed significant black shank symptoms, including severe wilting, necrosis, and stalk rot. Table 4.1 shows the number of plants rated in each group on each observation date.

Mean spectral profiles were calculated for each health rating on each observation date and plotted using SigmaPlot 12.3 (Systat Software, Inc., San Jose, CA). Areas within the mean spectral profiles were investigated statistically using PROC T-test in SAS statistical software (SAS Institute, Cary, NC) and indices were developed based on these differences. Differences in index values between asymptomatic and symptomatic plants were evaluated using ANOVA. In order to assess the ability to detect black shank incidence pre-symptomatically, two new separate groups of spectral profiles from the Aug. 2 dataset were organized to conduct a pre-symptomatic test. The healthy group consisted of all of the plants that were rated asymptomatic on Aug. 2 and Aug. 9 and the pre-symptomatic group contained plants that were rated asymptomatic on Aug. 2 but rated symptomatic on Aug. 9. Mean spectral profiles of the pre-symptomatic detection groups were plotted and the index values were statically analyzed using ANOVA.

The symptomatic and pre-symptomatic data sets were used to train supervised machine learning classification algorithms in Matlab (MathWorks, Inc., Natick, MA). Supervised machine learning algorithms use predictor variables (in this case health ratings) and a set of response variables (hyperspectral reflectance values) to train a model to make predictions about new data. A total of 22 supervised machine learning algorithms were trained with the data and subspace linear discriminant analysis (LDA) was chosen as the model with the best accuracy.

Subspace LDA is a machine learning algorithm that uses principle component analysis (PCA) as a preprocessor to reduce the dimensionality of the data before using LDA to find a linear transformation which minimizes the scatter within groups and maximizes the scatter between groups (Prasad & Bruce, 2008). A key output of subspace LDA is the confusion matrix, which is designed to display the amount of correct and incorrect predictions for each group and allow for calculation of performance statistics for a given model. An example of the confusion matrix output from Matlab is shown below.

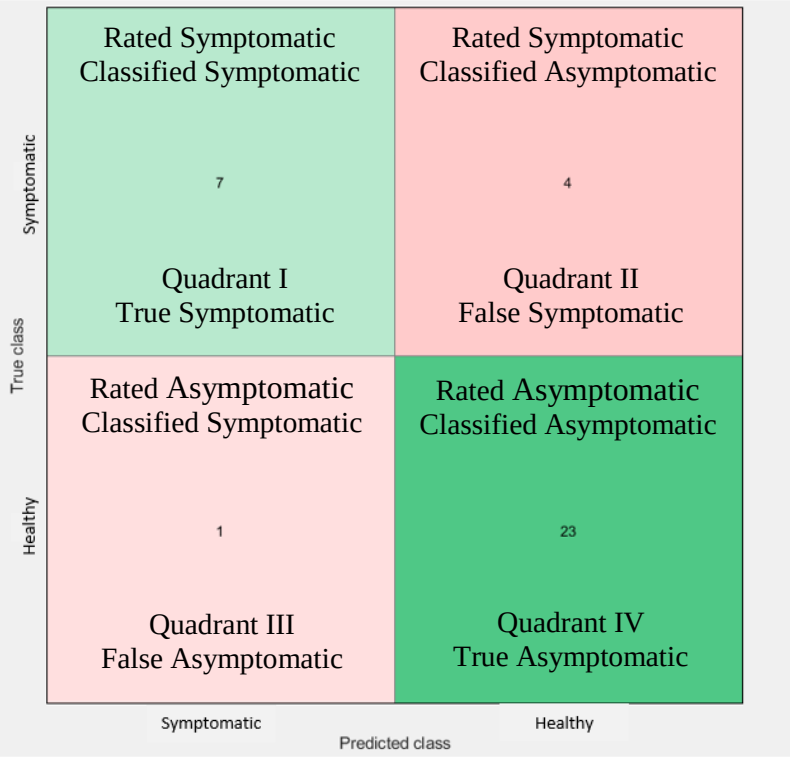

Quadrant 1 shows the number of true symptomatic predictions. In this study, the true symptomatic predictions are the measurements which were visually rated symptomatic and correctly classified as symptomatic by subspace LDA. False symptomatic predictions, in quadrant 2, are measurements that were visually rated symptomatic but incorrectly classified as asymptomatic. False asymptomatic predictions, in quadrant 3, are measurements that were

visually rated asymptomatic but classified as symptomatic. Quadrant 4 contains the number of true asymptomatic predictions, those measurements that were visually rated asymptomatic and correctly classified as asymptomatic by subspace LDA. Darker shades of red or green in each quadrant of the confusion matrix indicate increasing prediction values for that quadrant. An important measure of a supervised classification's performance is classification accuracy. Classification accuracy is defined as the number of true predictions divided by the total number of predictions times 100. Precision, recall, and F1 score are three additional performance measures used for analyzing the strength and accuracy of a supervised classification model. Precision is the number of true symptomatic predictions divided by the number of true symptomatic predictions and false symptomatic predictions, and a low precision value indicates a high amount of false symptomatic predictions in relation to true symptomatic predictions. In this case, a low precision value would mean the model did not classify symptomatic plants accurately. Recall is the number of true symptomatic predictions divided by the number of true symptomatic predictions and false asymptomatic predictions. A low recall means there is a large number of false asymptomatic predictions in relation to true symptomatic predictions. The F1 score is a statistic that measures the balance between precision and recall. A low F1 score indicates unbalance between the two. The formula is given below.

$$\text{F1 Score} = 2 \times \frac{precision \times recall}{precision + recall}$$

A follow-up field study was conducted in a *Ralstonia solanacearum* (Granville wilt) infested flue-cured tobacco production field near Kenbridge, VA. The same equipment was used as that in the black shank study. The protocol was the same except that the number of plants measured was 20. Health ratings used were asymptomatic, symptomatic, and diseased. The

objective was to examine the mean spectral profiles of black shank and Granville wilt infected plants to evaluate whether a hyperspectral index developed to detect black shank symptoms would be specific to black shank. Data was collected on Sept. 2, Sept. 11, and Sept. 18, 2018. This was after the removal of terminal inflorescence and directly prior to final harvest.

Results and Discussion

Evaluation of mean spectral profiles

Mean spectral profiles from the first observation date of the black shank study showed differences in the disease rating groups (Figure 4.3). The reflectance in the visible range (550 - 675 nm) increased with disease symptom expression. In the NIR range (700 - 1500 nm), the reflectance of the heathy plants was lower than that of the symptomatic and diseased group. However, the symptomatic group had the highest reflectance. Reflectance in the SWIR range (1500 - 2500 nm) followed the same trends seen from 550 - 675 nm.

The diseased group was comprised of severely infected plants and exhibited the same spectral characteristics as the symptomatic group, only with more pronounced increases in reflectance, compared to the mean spectral profiles of the asymptomatic plants on the first observation date (Fig. 4.3). Detecting black shank incidence as soon as possible was important. Therefore, only the asymptomatic and symptomatic groups were analyzed further. The reflectance in the SWIR (1500 - 2500 nm) followed similar trends as reflectance in the visual range. Sensors and cameras that measure only in the visual and NIR range are considerably less expensive than those that measure SWIR reflectance. There is value in make any proposed index relevant to future research and industry uses at the lowest possible cost. For these reasons, the

spectral range that was chosen for index development was 350 - 1500 nm or the visible and NIR range.

The mean spectral profiles of the asymptomatic and symptomatic groups for each observation date are shown in Figure 4.4. As disease development and symptom expression continued to progress, individual plants would be reclassified from the asymptomatic group to the symptomatic group if visual symptoms were observed and plants that were reclassified from the symptomatic group to the diseased group were removed from the analysis. On each date, the mean spectral profiles represent plants rated asymptomatic or symptomatic on that specific observation date. Thus, in the visible range of the spectrum, the reflectance of each group stayed consistent throughout the study. The difference in reflectance between the spectral profiles of the asymptomatic and symptomatic groups, for all four observation dates, from 550 – 675 nm was significant (p <0.001). The reflectance in the NIR was less consistent and there was not significant differences between the groups. The NIR reflectance was higher for the symptomatic plants on Aug. 2 and Aug. 17, similar on Aug. 9, and lower on Aug. 13 when compared to the asymptomatic plants.

The mean spectral profiles of the healthy and pre-symptomatic groups on Aug. 2 (Fig. 4.5) show similar differences to those shown between asymptomatic and symptomatic groups. Pre-symptomatic plants were those that were reclassified as symptomatic at the following assessment. In the 550 - 675 nm range, the pre-symptomatic plants had a higher mean reflectance compared to healthy plants. The difference in reflectance over this range was not as large as seen in the mean spectral profiles of asymptomatic and symptomatic plants. The differences in NIR reflectance between the pre-symptomatic plants and healthy plants were not significantly different.

Definition and assessment of proposed indices

Two black shank detection indices were developed based on the differences in the mean spectral profiles between the symptomatic and asymptomatic groups. The first was a broad-band index with reflectance values averaged over broad ranges of the spectrum and the second was a narrow-band index with two distinct wavelength reflectance values. Values for both indices range from 0 to 1, with increasing values indicating increased probability of black shank incidence. The formulas for which are given below, where r_x equals reflectance (r) at wavelength in nm (x).

Broad-band Black Shank Index

$$\frac{Avg(r_{550}-r_{675})}{Avg(r_{750}-r_{1200})}$$

Narrow-band Black Shank Index

$$\frac{r_{625}}{r_{800}}$$

The significant differences in the 550 - 675 nm range (p <0.0001) and the lack of significant differences in the 750 – 1200 nm range, with respect to black shank symptoms, were the justification for wavelengths selection for the numerator and denominator of both indices. The numerator of the equation is related to changes in reflectance based on disease incidence, while the denominator is used as a normalizing factor.

The differences between the broad-band black shank index values for the asymptomatic and symptomatic group were significant for the first three observation dates (*alpha* = 0.05) and significant on the fourth observation date at p = 0.0754 (Table 4.2). For the narrow-band black shank index, the first three observation dates were also statistically significant (*alpha* = 0.05) with the fourth date being significant at p = 0.0548 (Table 4.3). The index values for the pre-symptomatic comparison had lower p-values than seen in the symptomatic comparison. However, for the pre-symptomatic comparison, the difference in the groups for the broad-band

and narrow-band index were significant at $p = 0.0640$ and $p = 0.0860$, respectively. The index values of both the asymptomatic and symptomatic groups increased over time using both indices, possibly due to increased ripening of the crop as well as increasing disease distribution and severity. Both indices performed similarly, with little variation in mean group values or significance between groups. The two indices had a high correlation between them (r = .99). If these indices were to be used with hyperspectral imagery to construct a precision management strategy, an index threshold classification could be performed on the hyperspectral image matrix to render a single-band image that is predictive of black shank distribution within the field.

Classification using subspace LDA

Index application coupled with threshold classification is one way to classify hyperspectral data for features such as black shank incidence. Another method to classify hyperspectral data is by using machine learning classification algorithms, such as subspace LDA. The performance measures of subspace LDA for symptomatic detection on all four observation dates, as well as the Aug. 2 pre-symptomatic data set, is shown in Table 4.4. These values were calculated using the confusion matrix for each data set. Classification accuracy was highest on the first observation date. However, all of the other observation dates in the symptomatic test, as well as the pre-symptomatic test, had a higher level of precision. That is, disease detections predicted by subspace LDA for the later observation dates turned out to be more frequently true. Precision is an important measure for any model used to make decisions about where to treat or not treat for black shank. The consequences of treating plants unnecessarily (false asymptomatic) adds to the cost of production, but failing to treat when needed (false symptomatic) will result in increased yield and quality loss to disease. The first observation date had a high classification accuracy and recall, which exhibits accuracy in correctly predicting plants that were visually

rated as heathy. However, a relatively high amount of false symptomatic predictions caused the model to have low precision, making this model less desirable. Although the second and third observation dates had a lower classification accuracy, the precision of these models was higher than the first observation date due to a higher percentage of symptomatic plants that were correctly predicted. The fourth observation date had a higher precision value than the first and also had the highest F1 score of the symptomatic comparison. The increased precision values for the last three observation dates may be due to the number of symptomatic plants, relative to asymptomatic plants, included in each dataset (Table 4.1). The black shank infestation spread, causing more plants to be rated as symptomatic and less plants to be rated asymptomatic as the observation period progressed. The pre-symptomatic model also had good results. A low number of false positives contributed to a high precision value. The model also had a relatively low number of false negatives which bolstered the classification accuracy and recall value. These results show that there is potential for machine learning algorithms, specifically subspace LDA, to be used in conjunction with hyperspectral cameras to predict symptomatic and pre-symptomatic black shank infestations in flue-cured tobacco in real-time.

Analysis of tobacco spectral response to Granville wilt

The mean spectral profiles of plants in a Granville wilt infested field are displayed in Figure 4.6. These data were taken using the same protocol as used in the black shank study. The purpose of this companion study was to investigate the spectral profiles of Granville wilt infested plants to determine if a proposed index or model to detect black shank incidence would be specific to black shank or relevant to a range of tobacco pathogens. The first observation date shows some of the same differences in mean spectral profile of asymptomatic and Granville wilt symptomatic plants shown by the black shank groups. Notably, an increased reflectance from

550 - 675 nm for the symptomatic plants. The second and third observation dates do not show any substantial difference in this range. The data suggest that the indices presented to detect black shank incidence would not be useful for detecting Granville wilt incidence. The difference in spectral response of Granville wilt infested plants, compared to that of plants infested with black shank, may be due to the fact that Granville wilt infested plants tend to exhibit less yellowing during disease progression than plants that are infested with black shank, which yellow rather rapidly.

Conclusions

Significant differences in the mean index values of black shank symptomatic plants and asymptomatic plants demonstrated the ability of hyperspectral data to facilitate identification of black shank incidence. The differences in the pre-symptomatic test were significant ($a = 0.10$) for both indices. One would not expect for the differences in the mean index values of the pre-symptomatic groups to be as large as that of the symptomatic groups. While the plants in the symptomatic group were visually different and separable, the plants in pre-symptomatic groups were not. The next step would be to apply the proposed indices to aerial imagery and generate an index threshold-derived map in order to test the ability of the indices to detect black shank incidence at scale. If successful, an index threshold-derived map could be useful for facilitating variable rate fungicide applications as well as predicting future black shank infestation severity and location.

The high amount of correlation between the broad-band and narrow-band black shank indices indicates that high spectral resolution, such as that of hyperspectral data, is not necessary for classification of black shank incidence. The broad-band black shank index may require a custom multispectral lens for application, since it is calculated using distinct wavelength ranges.

However, multispectral cameras are considerably less expensive than hyperspectral cameras available. This cost savings may make the broad-band index more practical and efficient for flue-cured tobacco growers and researchers.

Subspace LDA also proved to be an effective tool for detecting symptomatic and pre-symptomatic black shank incidence. The advantage of using machine learning, over index threshold-derived maps, is the increased ability of machine learning to be automated. Index threshold-derived maps will need user control to set threshold values, in most cases. However, the ability of the user to set a custom threshold is, in some ways, an advantage of index threshold-derived maps as a means to detect and manage black shank incidence. A particular machine learning model may not work in every situation and provides the user little control over precision. Conversely, index thresholds can be used dynamically by allowing the user to set different thresholds for each unique situation. By setting a conservative (low) threshold, the user can minimize the number of false symptomatic predicted plants. If used for a variable rate fungicide application, this may result in a number of healthy plants being treated. However, a minimal amount of symptomatic and pre-symptomatic plants would be left untreated.

References

Brownlee, J. (2018a). Classification Accuracy is Not Enough: More Performance Measures You Can Use. Retrieved on March 21, 2019 from https://machinelearningmastery.com/classification-accuracy-is-not-enough-more-performance-measures-you-can-use/.

Brownlee, J. (2018b). What is a Confusion Matrix in Machine Learning. Retrieved March 26, 2019 from https://machinelearningmastery.com/confusion-matrix-machine-learning/

Chen, T., Zhang, J., Chen, Y., Wan, S., & Zhang, L. (2019). Detection of peanut leaf spots disease using canopy hyperspectral reflectance. *Computers & Electronics in Agriculture, 156*: 677-683.

Daub, M., Lucas, G., Shew, H., Echandi, E., Main, C., Shoemaker, P.,… Schneider, S. (1990). Compendium of Tobacco Diseases. St. Paul, Minnesota: The American Phytopathological Society.

GISGeography. Multispectral vs Hyperspectral Imagery Explained. (2018, February 16). Retrieved on April 12, 2019 from https://gisgeography.com/multispectral-vs-hyperspectral-imagery-explained/

Jia, F., Liu, G., Ding, S., Yang, Y., Fu, Y., & Wang, Z. (2013a). Using leaf spectral reflectance to monitor the effects of shading on nicotine content in tobacco leaves. *Industrial Crops & Products, 51*: 444.

Jia, F., Liu, G., Liu, D., Zhang, Y., Fan, W., & Xing, X. (2013b). Comparison of different methods for estimating nitrogen concentration in flue-cured tobacco leaves based on hyperspectral reflectance. *Field Crops Research, 150*: 108-114.

Lu, J., Zhou, M., Gao, Y., & Jiang, H. (2018). Using hyperspectral imaging to discriminate yellow leaf curl disease in tomato leaves. *Precision Agriculture, 3*: 379.

Mahlein, A.-K., Oerke, E.-C., Steiner, U., & Dehne, H.-W. (2012). Recent advances in sensing plant diseases for precision crop protection. *European Journal of Plant Pathology, 1*: 197.

Moghadam, P., Ward, D., Goan, E., Jayawardena, S., Sikka, P., & Hernandez, E. (2017). Plant disease detection using hyperspectral imaging. *2017 International Conference on Digital Image Computing: Techniques and Applications (DICTA), Sydney, NSW, 2017*: p. 1-8.

Nagasubramanian, K., Jones, S., Sarkar, S., Singh, A. K., Singh, A., & Ganapathysubramanian, B. (2018). Hyperspectral band selection using genetic algorithm and support vector machines for early identification of charcoal rot disease in soybean stems. *Plant Methods, 14*(1): 1-13.

Polder, Gerrit, Pekkeriet, Erik, and Snikkers, Marco. (2013). A spectral imaging system for detection of botrytis in greenhouses, Figure 3. *EFITA-WCCA-CIGR Conference "Sustainable Agriculture through ICT Innovation", Turin, Italy, 24-27 June 2013.* Retrieved January 30, 2019

Prasad, S. & Bruce, L. (2008). Limitations of principal components analysis for hyperspectral target recognition. *IEEE Geoscience Remote Sensing Letters, 5*(4): 625.

Rouse Jr, J. W., Hass, R. H., Schell, J. A., & Deering, D. W. (1973). Monitoring vegetation systems in the great plains with ERTS. *Proceedings 3rd Earth Resources Technology Satellite (ERTS) symposium, Vol. 1, NASA SP-351, NASA, Washington, DC, USA*: p. 309-317.

Zhu, H., Chu, B., Zhang, C., Liu, F., Jiang, L., & He, Y. (2017). Hyperspectral imaging for presymptomatic detection of tobacco disease with successive projections algorithm and machine-learning classifiers. *Scientific Reports (Nature Publisher Group), 7*: 1.

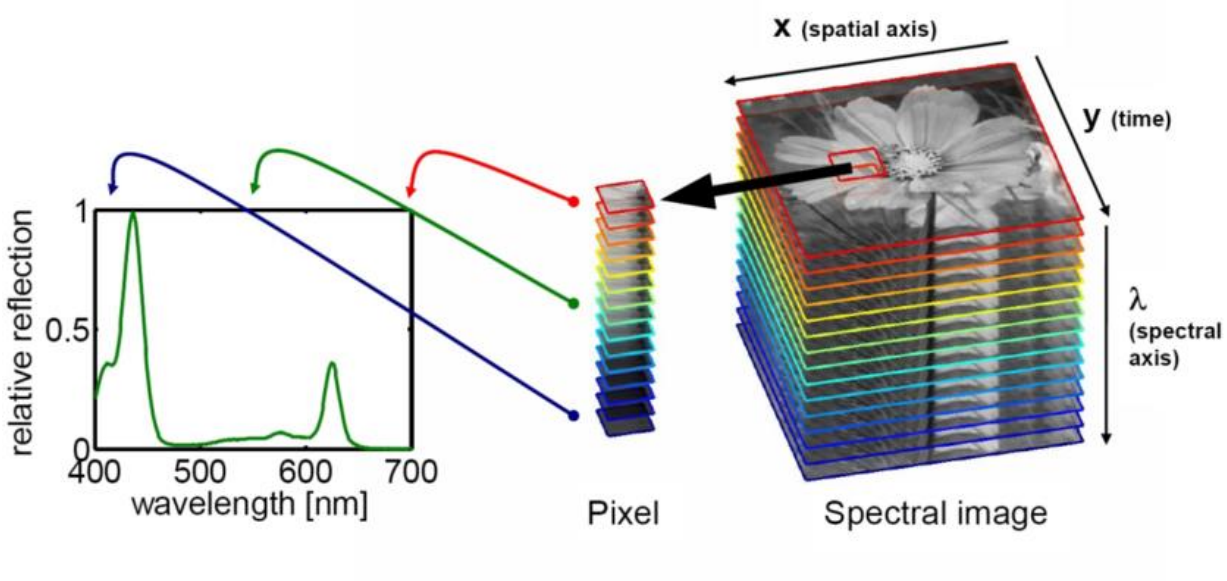

Figure 4.1- An example of a hyperspectral image data cube (right), a single pixel (center), and a point measurement or spectral profile (left) from Polder 2013. Hyperspectral image data cubes contain a stack of images, each containing the reflectance in a specific band of the spectrum. A spectral profile measured by a point measurement instrument, like a spectroradiometer, can be compared to one pixel of a hyperspectral image stack (Polder 2013).

Figure 4.2- Representative plants of each plant health rating for the black shank study conducted near Union Level, VA in 2018.

Table 4.1- Number of plants in each rating group for all observation dates of the black shank study conducted in Union Level, VA.

	Observation Date			
	Aug 2	**Aug 9**	**Aug 13**	**Aug 17**
Asymptomatic	25	8	8	8
Symptomatic	11	18	18	12
Diseased/Dead	4	14	14	20

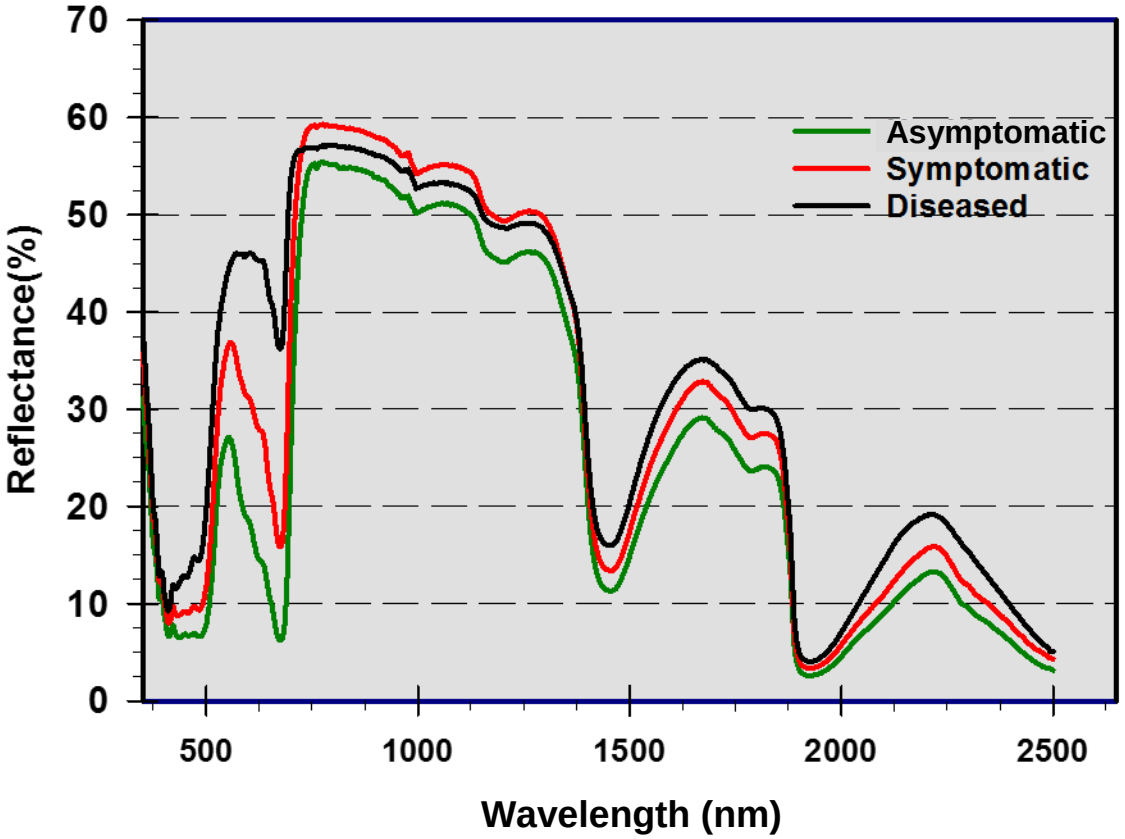

Figure 4.3- Mean spectral profiles of three disease rating groups in the black shank study conducted near Union Level, VA in 2018 at the first observation date (Aug. 2).

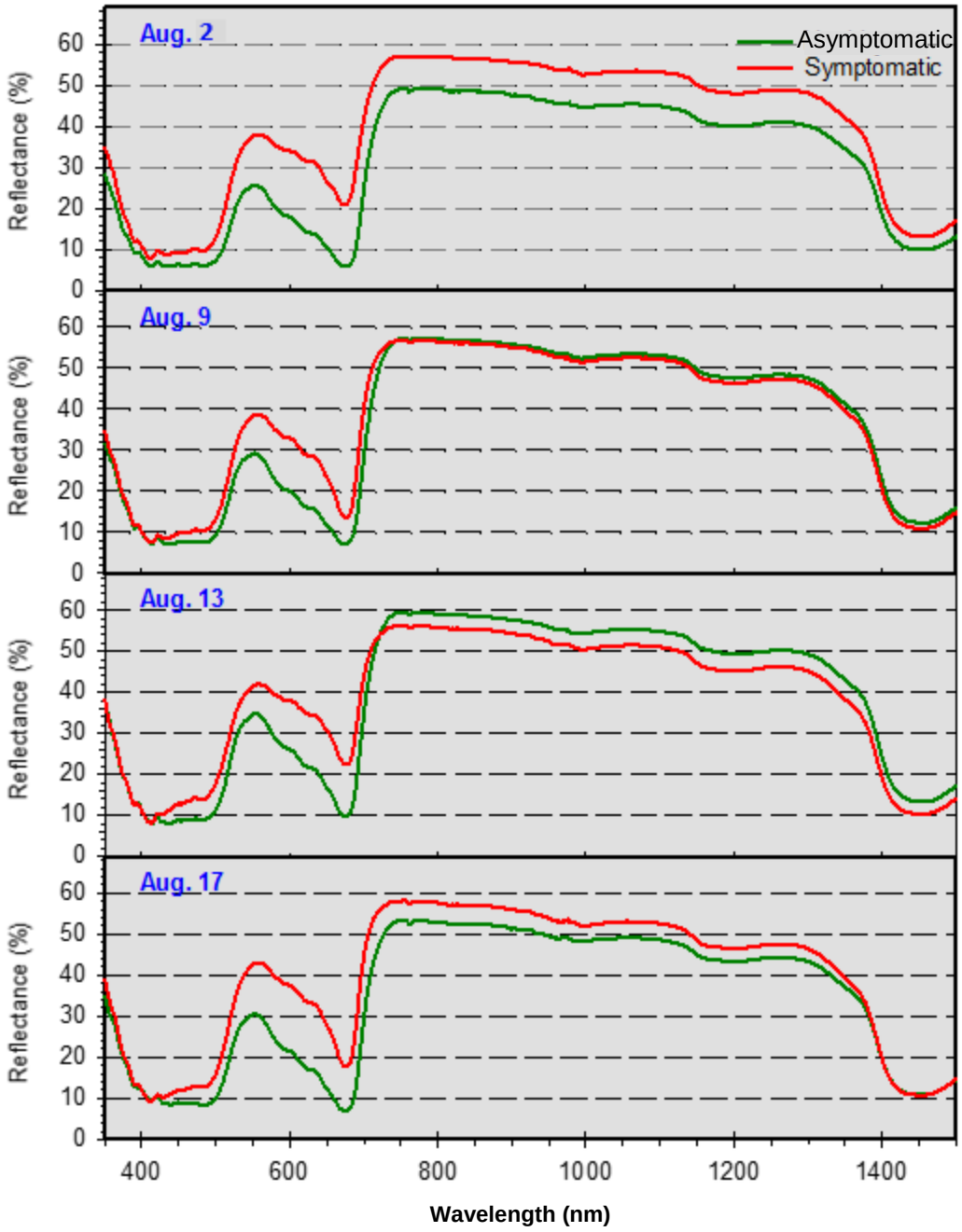

Figure 4.4- Mean spectral profiles of the black shank asymptomatic and symptomatic groups for all four observation dates of the 2018 black shank study conducted near Union Level, VA.

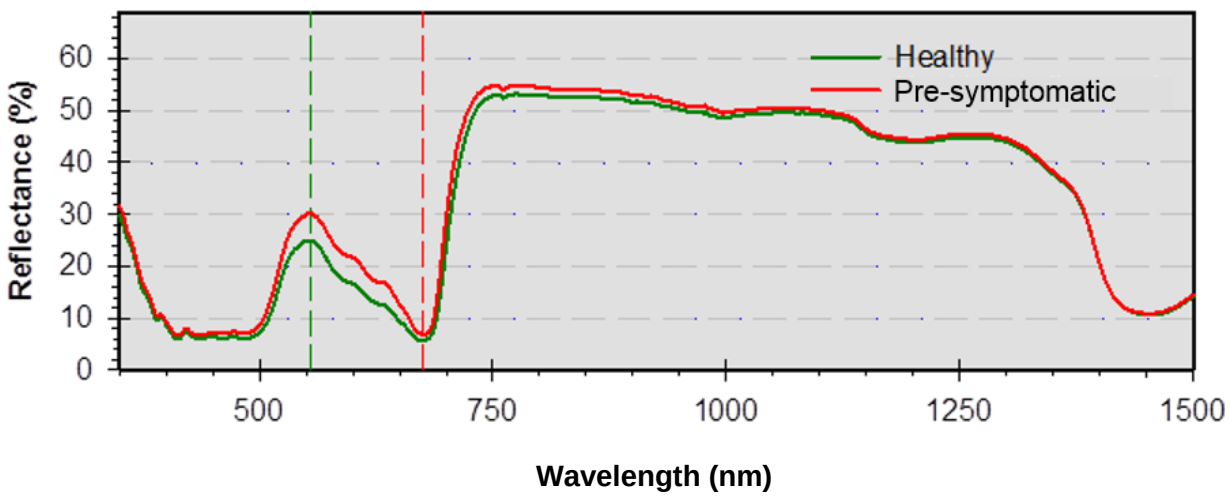

Figure 4.5- Mean spectral profiles of the two pre-symptomatic black shank detection groups. The data for the pre-symptomatic test was taken on the first observation date of the study (Aug. 2).

Table 4.2- Mean broad-band index values for asymptomatic and symptomatic groups, and the pre-symptomatic test grouping for pre-symptomatic plants healthy plants. The p-value indicates the significance of difference between the groups for each observation (paired T-test).

	Observation Date				
	Pre-symptomatic	Symptomatic			
	Aug 2	**Aug 2**	**Aug 9**	**Aug 13**	**Aug 17**
Mean Asymptomatic Index Value	0.2903	0.3193	0.3646	0.4462	0.4929
Mean Symptomatic Index Value	0.3644	0.5026	0.5330	0.6940	0.6204
p-value	*0.0640*	*0.0007*	*0.0008*	*0.0012*	*0.0754*

Table 4.3- Mean narrow-band index values for asymptomatic and symptomatic groups, and the pre-symptomatic test grouping for pre-symptomatic plants healthy plants. The p-value indicates the significance of difference between the groups for each observation (paired T-test).

	Observation Date				
	Pre-symptomatic	Symptomatic			
	Aug 2	**Aug 2**	**Aug 9**	**Aug 13**	**Aug 17**
Mean Asymptomatic Index Value	0.2333	0.2605	0.3062	0.3899	0.4269
Mean Symptomatic Index Value	0.3008	0.4643	0.4820	0.6420	0.5650
p-value	*0.0860*	*0.0004*	*0.0007*	*0.0015*	*0.0548*

Table 4.4- Performance measures for subspace LDA trained in Matlab for all observation dates, and the pre-symptomatic test, of the 2018 black shank study conducted near Union Level, VA.

	Observation Date				
	Aug 2	**Aug 9**	**Aug 13**	**Aug 17**	**Aug 2 Pre-Symptomatic**
Classification Accuracy	85.7%	61.5%	69.2%	75.0%	78.3%
Precision	0.64	0.72	0.78	0.77	0.81
Recall	*0.88*	*0.72*	*0.78*	*0.83*	*0.87*
F1 Score	*0.74*	*0.72*	*0.78*	*0.80*	*0.84*

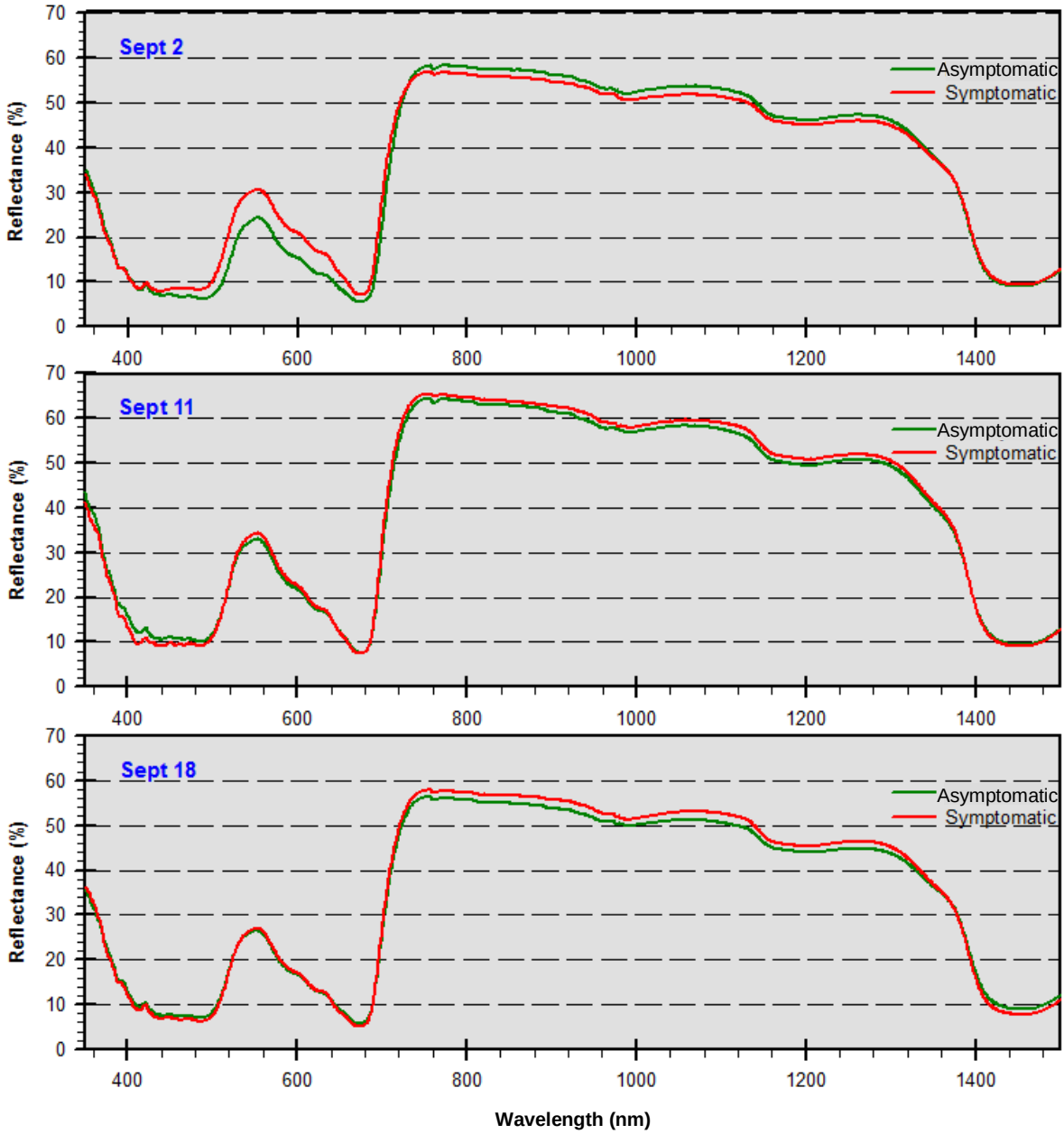

Figure 4.6- Mean spectral profiles of the asymptomatic and symptomatic groups for all three observation dates of the 2018 Granville wilt study conducted near Kenbridge, VA.

Chapter V

Conclusions and Future Direction

Evaluating UAV-acquired imagery's potential in flue-cured tobacco systems

UAV-acquired ENDVI surveys showed the ability to differentiate N-rates and varieties of flue-cured tobacco at and after topping. Collecting the images with the UAV and imagery post-processing was made relatively easy by using flight control and post-processing software. The visual surveys provided a detailed overview of the study area in less time than the area could be studied by foot. Further, the ENDVI surveys made stressed areas of the field easier to identify. These benefits are amplified if the technology is used in a larger growing area such as a production field. The most difficult and time-consuming process in the analysis was using zonal statistics to extract mean ENDVI values for each plot, because of the large number of small plots included in the experiment. Researchers will benefit from mean plot values. However, for producers, ENDVI maps or surveys may be sufficient for diagnosing problems and prescribing precise treatments.

In the future, radiometric correction would be beneficial for similar research or production applications. Radiometric correction uses either radiometric calibration panels placed in the survey area or a sunlight irradiance sensor mounted on top of the UAV to normalize surveys based on sunlight irradiance. Radiometric correction allows for temporal measurements to be compared accurately by minimizing variations in reflectance that are due to sunlight intensity. When comparing the 2017 surveys to the 2018 surveys, the need for radiometric calibration is obvious. The data for 2017 was taken in full sunlight, while the data for 2018 was taken with full cloud cover. The overall ENDVI mean of all observation dates for 2018 was .21

lower, a 51% drop, when compared to that of 2017. Although each year's data was taken in respect to cloud conditions and near solar noon, without radiometric correction, there is no way to know how much of the variability in the temporal trends of the data are a result of variations in sunlight irradiance.

UAV-acquired imagery is well suited for rapid and detailed scouting of flue-cured tobacco. One may use ENDVI surveys to identify and treat a specific problem area. There is no evidence that integration of UAV-based maps to apply layby fertilizer to flue-cured tobacco at a variable rate would be efficient or beneficial. However, given the significant differences in ENDVI values for flue-cured tobacco N-rates, doing so may increase input efficiency and yield by applying more fertilizer to areas with lower ENDVI values and less to areas with higher ENDVI values.

Hyperspectral imagery's potential for detection of black shank

Two spectral indices for detecting black shank incidence in flue-cured tobacco were introduced. They are based on significant differences found in the spectral profiles of healthy plants and those that showed early black shank symptoms. Furthermore, these indices show the potential to be used to identify black shank incidence pre-symptomatically. The next step would be to further evaluate these indices applying them to aerial imagery of a flue-cured tobacco field that is invested with black shank. The purpose of this research would be to investigate the feasibility of using a disease stress map derived from index threshold masking as a black shank detection strategy in commercial applications. If accurate detection using aerial imagery is possible, then it would be plausible to use the disease stress map generated for input into variable

rate spraying equipment. By applying fungicide at a variable rate, input costs of spraying application could be reduced.

Machine learning classification algorithms, such as subspace LDA, could also be a viable strategy for detecting black shank incidence. The major advantage that machine learning classification offers over index threshold masking is the ability to be automatic and used with very little user interaction. However, there are several disadvantages to using machine learning classification to identify black shank and apply variable rate treatment. The model's precision, with regards to correct prediction of black shank incidence, is not as controlled as when applying an index threshold. Subspace LDA will construct a model with the highest possible classification accuracy. However, we can assume that it would be better to treat plants without black shank symptoms than to leave plants with black shank symptoms untreated. For this reason, precision, or the percentage of symptomatic plants predicted correctly, is the best test of model's reliability for variable rate fungicide application. As the results of Chapter IV show, this precision value can vary even within the same field when using subspace LDA. The classification accuracy and precision may also be influenced by crop stage or variety.

Index threshold-derived stress maps offer more control over the precision of a variable rate treatment primary due to the user selection of threshold placement. If one is interested in treating black shank at a variable rate, but does not want to leave any symptomatic plants untreated, they would simply set the index threshold at a fairly conservative (lower) level with respect to the average index values of symptomatic and healthy plants. Similarly, if maximizing fungicide efficiency is of great importance, a more aggressive (higher) threshold could be set. The ability to set a custom threshold makes index threshold-derived stress maps more adaptable to flue-cured tobacco growth stage and varietal differences.

Appendix A

Mean ENDVI values for all varieties included in study on each observation date of 2017

	Variety										
DAT	**K 326**	**K 326 pYLW**	**NC 196**	**PVH 1118**	**PVH 1452**	**PVH 1600**	**PVH 1920**	**PVH 2110**	**PVH 2254**	**PVH 2310**	**p-value**
36	0.2683	0.2755	0.2536	0.2658	0.2748	0.2721	0.2673	0.2742	0.2713	0.2642	*0.4990*
43	0.3548	0.3636	0.3512	0.3598	0.3724	0.3697	0.3625	0.3674	0.3561	0.3602	*0.6172*
46	0.3972	0.4041	0.3912	0.3978	0.4040	0.4065	0.3965	0.4063	0.4027	0.4024	*0.9182*
53	0.4031	0.4057	0.3994	0.4025	0.4110	0.4223	0.4150	0.4094	0.4146	0.4103	*0.1191*
59	0.4810	0.4830	0.4818	0.4763	0.4848	0.4968	0.4895	0.4875	0.4909	0.4825	*<0.0001*
67	0.5406	0.5389	0.5502	0.5389	0.5491	0.5554	0.5483	0.5504	0.5455	0.5416	*<0.0001*
71	0.4687	0.4683	0.4718	0.4644	0.4759	0.4860	0.4801	0.4755	0.4730	0.4648	*<0.0001*
74	0.4540	0.4548	0.4525	0.4473	0.4558	0.4684	0.4588	0.4603	0.4622	0.4522	*0.0015*
79	0.4148	0.4146	0.4135	0.4095	0.4178	0.4259	0.4259	0.4190	0.4217	0.4091	*<0.0001*
81	0.4015	0.3980	0.4030	0.3922	0.4053	0.4120	0.4076	0.4067	0.4053	0.3883	*<0.0001*
85	0.5068	0.5082	0.5054	0.5015	0.5080	0.5213	0.5118	0.5133	0.5142	0.4946	*<0.0001*
89	0.4427	0.4489	0.4408	0.4364	0.4429	0.4551	0.4484	0.4536	0.4568	0.4256	*<0.0001*
93	0.4576	0.4597	0.4533	0.4453	0.4517	0.4634	0.4597	0.4603	0.4721	0.4339	*<0.0001*
95	0.3689	0.3689	0.3624	0.3531	0.3623	0.3706	0.3688	0.3701	0.3797	0.3488	*<0.0001*
103	0.3636	0.3646	0.3566	0.3476	0.3518	0.3619	0.3615	0.3643	0.3780	0.3431	*<0.0001*
107	0.3708	0.3722	0.3612	0.3534	0.3594	0.3642	0.3653	0.3725	0.3866	0.3447	*<0.0001*
125	0.3873	0.3816	0.3717	0.3601	0.3680	0.3697	0.3705	0.3771	0.3913	0.3553	*<0.0001*

Appendix B

Mean ENDVI values for N-rates on each observation date of 2017

	N-rate			
DAT	**Low**	**Medium**	**High**	**p-value**
36	0.2689	0.2658	0.2715	*0.5601*
43	0.3648	0.3628	0.3577	*0.4553*
46	0.4121	0.3950	0.3956	*0.0063*
53	0.4117	0.4066	0.4097	*0.4812*
59	0.4838	0.4845	0.4880	*0.0006*
67	0.5414	0.5466	0.5497	*0.0005*
71	0.4672	0.4737	0.4777	*0.0002*
74	0.4510	0.4575	0.4614	*0.0004*
79	0.4121	0.4159	0.4237	*<0.0001*
81	0.3966	0.4046	0.4048	*<0.0001*
85	0.5054	0.5075	0.5127	*0.0270*
89	0.4440	0.4445	0.4469	*0.1904*
93	0.4486	0.4541	0.4635	*<0.0001*
95	0.3600	0.3654	0.3706	*<0.0001*
103	0.3537	0.3578	0.3663	*<0.0001*
107	0.3608	0.3616	0.3727	*<0.0001*
125	0.3655	0.3722	0.3822	*<0.0001*

Appendix C

Mean ENDVI values for all varieties included in study on each observation date of 2018

	Variety									
DAT	**K 326**	**NC 196**	**PVH 1452**	**PVH 1600**	**PVH 1920**	**PVH 2110**	**PVH 2254**	**PVH 2275**	**PVH 2310**	**p-value**
34	0.0582	0.0604	0.0632	0.0622	0.0600	0.0621	0.0616	0.0604	0.0642	*0.7687*
54	0.2463	0.2516	0.2637	0.2655	0.2523	0.2630	0.2721	0.2598	0.2678	*0.1446*
61	0.2685	0.2756	0.2780	0.2803	0.2773	0.2814	0.2942	0.2790	0.2836	*0.7482*
67	0.2113	0.2099	0.2132	0.2132	0.2178	0.2130	0.2234	0.2222	0.2134	*0.4717*
76	0.2398	0.2344	0.2361	0.2395	0.2388	0.2424	0.2451	0.2412	0.2323	*0.7938*
99	0.1656	0.1608	0.1617	0.1706	0.1715	0.1706	0.1809	0.1688	0.1492	*<0.0001*
116	0.2415	0.2307	0.2282	0.2388	0.2343	0.2452	0.2676	0.2363	0.2085	*<0.0001*
127	0.1698	0.1550	0.1524	0.1603	0.1667	0.1687	0.1841	0.1669	0.1312	*<0.0001*

Appendix D

Mean ENDVI values for N-rates on each observation date of 2018

	N-rate			
DAT	**Low**	**Medium**	**High**	**p-value**
34	0.0588	0.0635	0.0618	*0.0466*
54	0.2442	0.2693	0.2672	*<.0001*
61	0.2619	0.2849	0.2926	*0.0001*
67	0.2069	0.2188	0.2201	*0.0021*
76	0.2270	0.2419	0.2476	*<.0001*
99	0.1665	0.1624	0.1709	*0.0009*
116	0.2372	0.2320	0.2411	*0.0251*
127	0.1630	0.1577	0.1643	*0.1932*

Appendix E

Daily rainfall amounts (inches) for 2017 and 2018 tobacco growing season

	2017					2018				
	MAY	**JUN**	**JUL**	**AUG**	**SEP**	**MAY**	**JUN**	**JUL**	**AUG**	**SEP**
1	-	0.00	0.00	0.00	0.73	-	0.01	0.00	0.01	0.19
2	-	0.00	0.00	0.00	0.17	-	1.34	0.00	0.61	0.01
3	-	0.00	0.00	0.00	0.01	0.00	0.40	0.00	0.25	0.00
4	-	0.06	1.20	0.00	0.00	0.00	0.00	0.00	0.00	0.00
5	-	0.60	0.00	0.00	0.00	0.00	0.00	0.21	0.00	0.00
6	-	0.00	0.48	0.00	0.29	0.00	0.00	1.63	0.00	0.00
7	0.01	0.00	0.06	0.00	0.01	0.00	0.00	0.05	0.06	0.00
8	0.00	0.00	0.00	3.25	0.00	0.00	0.00	0.00	0.02	-
9	0.00	0.00	0.00	0.00	0.00	0.00	0.00	0.00	0.00	-
10	0.00	0.00	0.00	0.00	0.00	0.08	1.33	0.00	0.00	-
11	0.08	0.00	0.00	0.00	0.00	0.00	0.07	0.02	0.02	-
12	0.74	0.00	0.00	0.26	0.25	0.00	0.00	0.00	0.72	-
13	0.22	0.17	0.00	0.04	0.02	0.00	0.00	0.00	0.08	-
14	0.00	0.83	0.00	0.00	0.00	0.00	0.00	0.00	0.01	-
15	0.00	0.00	0.00	0.35	0.00	0.00	0.00	0.00	0.00	-
16	0.00	0.08	0.00	0.00	0.00	3.02	0.00	0.00	0.00	-
17	0.00	0.33	0.00	0.09	0.00	0.39	0.00	0.13	0.00	-
18	0.00	0.00	0.00	0.00	-	4.32	0.03	0.01	0.10	-
19	0.33	1.13	0.00	1.33	-	0.25	0.25	0.00	1.00	-
20	0.00	0.00	0.00	0.00	-	0.00	0.92	0.00	0.60	-
21	0.02	0.00	0.00	0.00	-	0.02	0.34	0.20	0.08	-
22	0.25	0.00	0.00	0.00	-	0.20	1.17	0.60	0.02	-
23	1.02	0.00	0.00	0.79	-	0.01	0.01	0.05	0.00	-
24	0.79	0.00	0.00	0.29	-	0.00	0.22	0.20	0.02	-
25	0.63	0.00	0.00	0.00	-	0.00	0.01	0.31	0.00	-
26	0.01	0.00	0.00	0.00	-	0.09	0.01	0.01	0.00	-
27	0.34	0.00	0.00	0.00	-	0.22	0.00	0.00	0.00	-
28	0.05	0.00	0.03	0.00	-	0.82	0.00	1.07	0.00	-
29	0.01	0.00	0.05	1.40	-	0.03	0.00	0.20	0.00	-
30	0.00	0.00	0.00	0.00	-	0.04	0.00	1.24	0.85	-
31	0.00	-	0.00	0.00	-	0.04	-	0.37	0.10	-